

Mesoscale Mechanics of Reactive Materials for Enhanced Target Effects

Final Report 2012

Report I-69/12

Prepared by:

G. Heilig
N. Durr
M. Sauer
A. Klomfass

Management:

A. Klomfass

January 2013
Freiburg, Germany

Mesoscale Mechanics of Reactive Materials for Enhanced Target Effects

Final Report 2012

Report I-69/12

Ordering Customer

Office of Naval Research

Project Number (EMI)

277 118

Award Number

N00014-11-1-0307

Classification

Restricted Distribution

Prepared by:

Dr. G. Heilig

Research Fellow – Computational Physics

N. Durr

Research Fellow – Computational Physics

Dr. M. Sauer

Group Manager – Computational Physics

Management:

Dr. A. Klomfass

Principal Investigator

Prof. Dr.-Ing. S. Hiermaier

Head of Department – Dynamics in Microstructures

Prof. Dr. K. Thoma

Director of Ernst-Mach-Institut

Table of Contents

1	Introduction	4
1.1	Objectives	4
1.2	Review of Achievements 2007–2009	4
1.3	Overview and Summary 2011–2012	6
2	Boundary Conditions for explosive Launch	10
2.1	Objectives and Approach	10
2.2	Materials and Computational Model	10
2.3	Results of 2-D Simulations	12
2.4	Results of 3-D Simulations	20
3	Mesoscale Material Modeling	23
3.1	Mesoscale Material Structures	23
3.2	Computational Models and Material Properties	27
3.3	Geometrical Scaling on the Macroscale	29
3.4	Fragment Size Analysis	30
4	Mesoscale Launch Simulations and Analysis	32
4.1	Launch Modeling	32
4.2	Launch Simulation Results	33
5	Mesoscale Impact Simulations and Analysis	55
5.1	Impact Modeling	55
5.2	Impact Simulation Results	56
6	Further Impact Conditions	65
7	Validity of the Scaling Concept	74
7.1	Assessment for Tensile Test Simulations	74
7.2	Assessment for Impact Simulations	78
7.3	Assessment for Launch Simulations	79
8	Literature	83

1 Introduction

1.1 Objectives

Fraunhofer EMI received two grants from the Office of Naval Research dedicated to the investigation of the mechanical behavior of reactive materials on the mesoscale: a first grant awarded in June 2007 for a performance period until December 2009, and the current grant awarded in March 2011 for a performance period until September 2012.

The objectives were to develop (first grant) and to apply (second grant) suitable methods for the analysis and prediction of fragmentation of reactive materials. Such methods can be used to support the design of materials for specific applications, e. g. by selecting suitable values for parameters like grain size distribution, porosity, sintering pressure and temperature.

Specifically, the projects were motivated by the aim to design metallic materials, which fragment under certain dynamic loading conditions into small particles, which can chemically react with a suitable ambient medium, such as shock-heated ambient air or hot detonation products. Such materials could be effectively used to devise new or improved weapons with enhanced mechanical and/or thermal effects, see Figure 1.1.

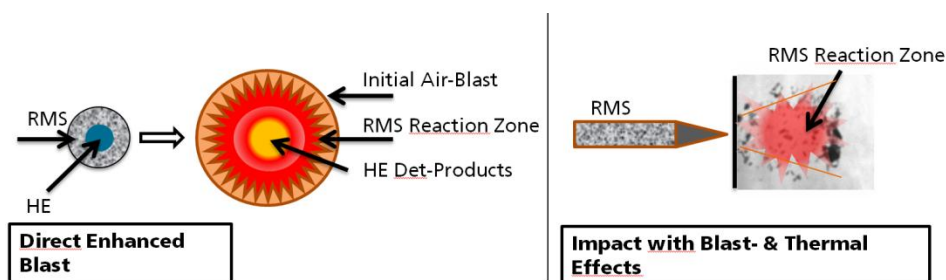


Figure 1.1: Two principle applications of reactive material structures (RMS) in which a fine fragmentation is crucial for enhanced weapon effects.

1.2 Review of Achievements 2007–2009

The objective of the first project was the development and validation of computational methods for the mechanical simulation of materials at grain scale. These methods shall enable the predictive analysis of the dependencies of the mechanical properties - especially the fragmentation behavior - on the morphological and constitutive nature of a material at grain scale. The development of computational methods covered two aspects:

- Algorithms for the parameter-controlled generation and meshing of representative volume elements (RVEs) with realistic microstructures.
- A finite-element solver for three dimensional time dependent continuum mechanical simulation of the response of a RVE to external loads, including inter-granular failure and fragmentation.

Suitable methods for both aspects were further developed towards the required capabilities during the project.

Furthermore, an experimental investigation on selected inert reference materials was performed for the validation of the developed methods. This included the selection and procurement of the materials, microstructural analysis and conduction of various characterization tests, particularly the conduction of fragmentation tests.

The results achieved can be summarized as follows (c.f. [1,2]): Copper (Cu) and Iron (Fe) powders were selected as inert reference materials. From these materials, a variety of cold-pressed and subsequently sintered samples with different porosities were produced. Mixtures of CuFe (50:50 by volume) were also manufactured. Material characterization was achieved by static and dynamic tensile tests, impact tests such as inverse Taylor tests and planar plate tests, and cube impact tests on aluminum plates. The experimental results served as a basis for the mesomechanical modeling, in particular for the identification of mesoscale material parameters and for model validation.

RVEs were generated based on statistical evaluation of micrographs taken from the material samples. The commercial software GEODICT (Fraunhofer ITWM) was used for that purpose. In addition, the new software GEOSTAT was developed, which is particularly capable of constructing parameter-controlled RVEs for the investigated microstructures.

Material model parameters were deduced from the static tensile tests. The mechanical properties of the metallic grains and the grain boundaries were chosen such that simulated stress-strain curves reproduced the experimental measurements. As a validation step, a homogenized (continuum) material model was derived from the mesomechanical simulations and was used to simulate compression tests on the macroscale.

The fragmentation characteristics of three material variants were analyzed in mesomechanical cube impact simulations. A good qualitative accordance with experimental observations was reached.

As simulation tool, the commercial software LS-DYNA had been used. In addition, the finite-element code MESOFEM, which has been developed at Fraunhofer EMI, has been adapted and extended such that it could be used for the simulation of fragmentation processes in sintered metallic materials.

1.3 Overview and Summary 2011–2012

The current project was focused on application, as it particularly considered the potential improvement of the effectiveness of anti-aircraft or anti-missile warheads by using reactive materials in warhead casings.

Although a number of candidate materials have been proposed for this purpose, e.g. mixtures of PTFE and aluminum, [3], the development of a practically usable material is still an open issue as it must combine several properties:

- sufficient strength to withstand explosive launch from warhead,
- sufficient weight for effective perforation,
- fine grained fragmentation upon impact,
- reactivity of fragments,
- reasonable production costs.

Sintered metallic powders are potential candidates and offer a number of adjustable properties which depend on the raw materials they consist of (e. g. aluminum, magnesium and tungsten), their initial state (e. g. grain size distribution) and fabrication parameters (e. g. pressures and temperatures applied during sintering).

A promising choice for the reactive material constituents are aluminum and tungsten. Tungsten offers a high ballistic effectiveness while aluminum provides high reactivity. This combination was therefore chosen for further investigation in this project.

The specific aim of the research was the identification of suitable microstructures of tungsten-aluminum mixtures by means of computational mesoscale analyses. These microstructures shall survive an explosive launch in a conventional warhead, effectively perforate a thin target and fragment into very small particles upon perforation of the target.

Figure 1.2 gives an overview on the conducted research.

A first status report has been delivered to ONR as part of a written overview for the 2011 peer review of the *ONR 351 Advanced Energetic Materials and Advanced Combustion Program*, [4]. An interim report, [5], was delivered in January 2012. Results have also been presented and published in the peer-reviewed proceedings of the 12th Hypervelocity Impact Symposium, [6]. The present report is the final for the current project.

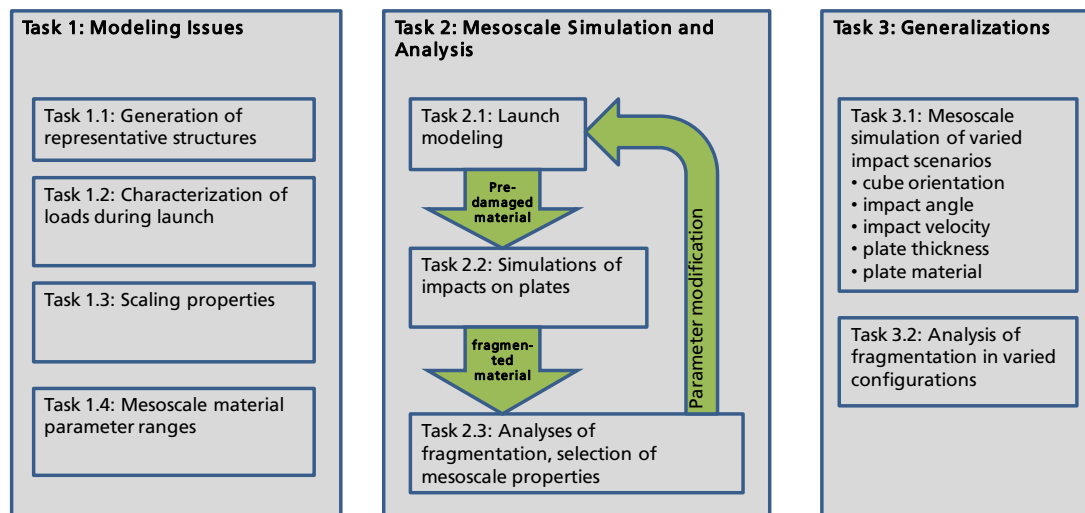


Figure 1.2: Overview on the tasks in the project 2011–2012.

Task 1.1 addressed the generation of representative material structures with different grain size distributions, porosities and material compositions. The software GEOSTAT developed in the previous project was applied for this purpose.

In task 1.2, the fluid dynamic loading conditions exerted on a considered pre-fabricated cubic fragment during the explosive launch from the warhead were determined in macroscale simulations of the launch process. The ANSYS-AUTODYN software with fluid-structure interaction was used for this task.

The metal cube considered as an example of a pre-fabricated fragment had an edge length of 1 cm and was composed of grains with average size of about $30\text{ }\mu\text{m}$ – $40\text{ }\mu\text{m}$. As an adequate spatial resolution of the entire cube on the mesoscale was computationally not possible (about 20–40 billion elements would be required), geometrical scaling on the macroscale had to be applied; grain sizes are kept at true scale in this approach while the dimensions of the cube and the target plate are reduced. The chosen scale was 1:33. The scaling approach was used in both launch and impact analyses. Its validity was checked in task 1.3 through comparison with selected simulations on larger scales (1:16 and 1:11).

In task 1.4 the parameters of the mesoscale material models for aluminum and tungsten were obtained from literature. The models consisted of elastic-plastic stress-strain relations with linear hardening for the bulk grain materials and also for the inter-granular boundaries. For the latter, different parameter sets were used to represent different inter-granular strength properties, as these may be adjusted by choosing suitable sintering temperature and pressure in a fabrication process. A particular element of the computational model was the node-splitting approach, which was used to treat inter-granular failure. This approach was developed in the previous project. Intra-granular failure was excluded in the applied models.

Task 2 was dedicated to a systematic parameter variation with the aim to identify a material that survives the explosive launch and fragments appropriately upon perforation of the chosen target, a 1 mm aluminum plate. For this purpose, mesoscale simulations of the scaled launch and the scaled impact process were performed for the various materials defined in tasks 1.1 and 1.4. The mesoscale simulations were performed with LS-DYNA.

In task 3 the impact simulations were extended to further scenarios for a few selected materials. Variations with respect to impact velocity, target material and target orientation were considered.

The results obtained in this project can be summarized as follows:

- The computational analysis carried out in this project relies on the application of scaling on the macro scale. For the impact process a criterion could be deduced, which permits an assessment of the validity of the scaling. For the investigated materials and impact conditions, the applied scaling factor (1/33) satisfied this criterion (c.f. Chapter 7.2). However, no criterion was found with respect to the effect of the scaling in the launch simulations; the comparison with a simulation on a larger scale (1/16) revealed, that the used scaling factor might be too small for a reliable answer on whether the cube survives the explosive launch intact or not (Chapter 7.3). However, for the extensive parameter variations conducted in this study only the scaling ratio of 1/33 could be realized due to the enormous computational effort required for larger scaling factors.
- Six different mixture ratios ranging from pure tungsten to pure aluminum have been investigated in different mesostructural configurations (different grain size statistics, porosities and inter-granular strengths, c.f. Chapter 3). From these variants, only the pure tungsten materials and the mixture of 25 vol-% Al and 75 vol-% tungsten survived the simulated explosive acceleration from the warhead (Chapter 4).
- The materials which survived the simulated launch process were further investigated with respect to their capability for target perforation and fragmentation. All materials were found to perforate the investigated thin targets and to fragment to a large degree upon impact (Chapter 5). The fragmentation was assessed through evaluation of the average fragment size (Chapter 3.4). The Al25/W75 mixtures came close to total fragmentation, as the average fragment size almost equaled the average grain size (intra-granular fracture was excluded in the models).
- The investigation of further impact conditions (Chapter 6) revealed a robust fragmentation characteristic of the investigated Al25/W75 material. The dependency of the average fragment size on the impact conditions was mostly unambiguous. As an exception, the variation of the impact angle has shown a non-monotonic effect on the fragment size. As for its practical importance, this finding may need further investigation.

- The effects of porosity and inter-granular strength on the fragmentation upon impact have similar appearances. Increasing porosity and/or decreasing inter-granular strength both reduce the average fragment size.
- No significant differences of the fragmentation behavior could be distinguished between the two different grain size distributions investigated in this study. These distributions possessed rather narrow and rather wide grain size intervals (here called “uniform” and “non-uniform” distributions, c.f. Chapter 3.1).

The results can be summed up by the statement that it seems worthwhile to further investigate the material mixture Al25/W75 computationally as well as experimentally.

The application of an advanced computational method seems recommendable for this purpose, as the computational method applied in this study is not without drawbacks. Although the node-splitting approach permits a reasonable parameterization and treatment of inter-granular failure, undesired intra-granular cracks may be generated. Furthermore, a certain amount of element erosion occurs on inter-granular zones; in addition the hexahedral modeling results in stepwise approximated grain surfaces, which may also impair the quality of the predictions. Most of all, the treatment of larger scales would be desirable. The currently used version of LS-DYNA could – for the specific models of this study – be successfully run only in single core mode.

As a promising alternative, the MESOFEM code can be applied, which was specifically developed for this type of simulations, [7]. It was not ready for use when this project began, but has been furnished with the required methods and models during the last year and can now be used for a wide range of mesoscale material simulations.

2 Boundary Conditions for explosive Launch

2.1 Objectives and Approach

In order to determine realistic loading conditions for pre-formed fragments during explosive launch from a warhead casing, a generic warhead configuration is analyzed on the macroscale. The pressure-time histories obtained from the macroscale simulations were subsequently used as boundary conditions in the mesoscale simulations for the further analysis of the material response to this loading.

The simulations described in this chapter were performed with the commercial code ANSYS-AUTODYN. In order to evaluate the pressures acting on the pre-formed fragments during the explosive launch, we used a simplified model where material failure and erosion was excluded. In the macroscale model, the cubes are treated as homogenous bodies composed of a single material with properties of pure tungsten or pure aluminum or mixtures of these. The material properties of the four considered mixtures were obtained by volumetric averaging of the properties of tungsten and aluminum.

A two-dimensional simplified model of a warhead cross section was used for the analysis; the validity of this simplification has been checked by comparison with results obtained from a three-dimensional simulation for a selected case.

2.2 Materials and Computational Model

Figure 2.1 shows the numerical setup of the fully coupled Euler-Lagrange simulations in two dimensions. In total, 32 Lagrangian parts (dark blue) – representing cubes with 10 mm edge length and consisting of aluminum, tungsten or mixtures of these – are placed at a radius of 52.5 mm around a TNT cylinder (light blue). The detonation initiation point is on the axis of the TNT cylinder. The TNT and the air (green) are modeled in the Eulerian part, which ranges from -250 mm to 250 mm in x- and y-direction and consists of quadratic elements of 0.5 mm edge length. The Lagrangian parts, which represent the metal cubes, are also quadratic with a size of 10 mm and contain 10 elements in each direction (element edge length 1.0 mm). The resolution of the Eulerian part is thus twice as fine as that of the Lagrangian parts. The TNT is modeled using the JWL-equation of state with density $\rho = 1.63 \text{ g/ccm}$ and detonation velocity 6930 m/s. The air is treated as an ideal gas of constant specific heats (adiabatic coefficient $\gamma = 1.40$).

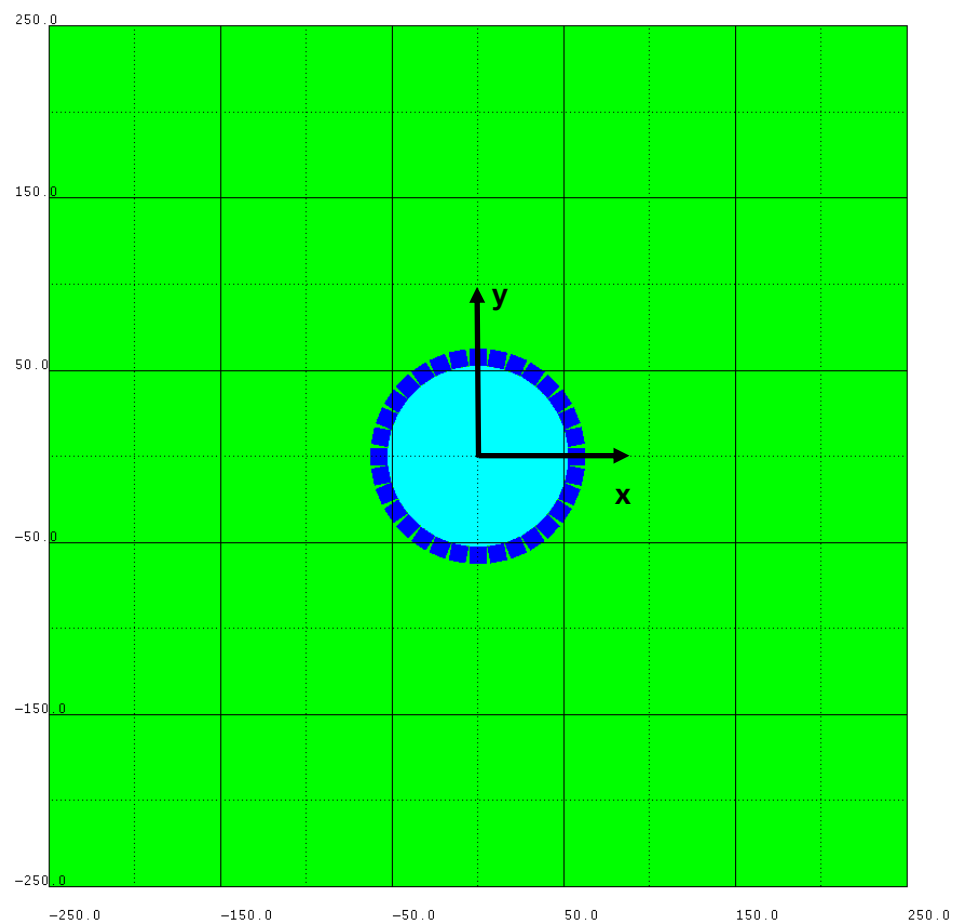


Figure 2.1: Numerical setup for the 2-D fluid-structure coupled simulation of the fragment acceleration.

The cube materials considered in the analysis were pure Aluminum (Al), pure Tungsten (W) as well as the four mixtures Al/W 25/75, Al/W 38/62, Al/W 50/50 and Al/W 83/17 further specified in Table 2.1.

A Mie-Gruneisen equation of state and the Steinberg-Guinan strength model was used for both materials, [8]. Failure and erosion were however not considered as the simulations solely aimed on the determination of the fluid dynamic loading of the pre-fabricated warhead fragments. The material parameters of the four mixture materials were estimated through volumetric averaging of the respective aluminum and tungsten parameters.

Table 2.1: Material parameters for the six mixtures (solid materials without pores). The constituents are Al7039 and tungsten.

	Al	Al/W 83/17	Al/W 50/50	Al/W 38/62	Al/W 25/75	W
Mass Ratios	100/0	5/95	8/92	13/87	42/58	0/100
Density [g/ccm]	2.77	5.52	11.04	13.02	15.17	19.30
Gruneisen Γ_0 [-]	2.00	1.944	1.84	1.795	1.75	1.67
C_1 [m/s]	5328.0	5107.34	4679	4523.24	4354.5	4030.0
S_1 [-]	1.338	1.321	1.29	1.2754	1.1623	1.237
Yield stress Y_0 [kPa]	3.37e5	6.5371e5	1.2685e6	1.492e6	1.734e6	2.2e6
Shear modulus G_0 [kPa]	2.76e7	5.011e7	9.38e7	1.097e8	1.269e8	1.6e8

2.3 Results of 2-D Simulations

The explosive launch was simulated for all six materials listed in Table 2.1 In order to evaluate the effect of porosity on the pressure loads, tungsten with 10 % and 20 % porosity was considered. The porosity was realized by removing elements from the interior of the Lagrangian parts, thus reducing the mass or average density of the cube.

Figure 2.2 shows examples of the computed flow fields in terms of isopycnics (lines of constant density) at two different times after initiation of the TNT. The propagation of the gaseous detonation products through the metallic cubes, the radial movement of the cubes and the build-up of the shock wave in the air can be clearly recognized. Although the setup is symmetric at time zero, the resulting air shock and the contact lines are not. This is a consequence of the fluid-dynamic instabilities and the finite approximation on the Cartesian grid.

Figure 2.3 shows three cubes in enlargement (above: aluminum; below: tungsten) at 40 μ s after initiation. Note that the aluminum cubes are strongly deformed while the tungsten cubes roughly keep their original shape.

In Figure 2.4 the cube velocities during the launch phase are shown for the different materials. After approximately 100 μ s, the acceleration tends to zero and the final velocity is reached. Due to the different masses (densities) of the cubes, the final velocities differ significantly. The final velocity of an aluminum cube is ca. 2010 m/s, while the tungsten cube reaches about 860 m/s. The final velocities of the cubes made of the Al/W mixtures and the porous tungsten fall consistently between the velocities of the pure aluminum and pure tungsten cubes.

For the evaluation of the fluid dynamic loading of the cubes, the gas pressure in the Eulerian mesh has been evaluated from gauges located near the center of the top, the side and the bottom faces of a selected cube (see Figure 2.3). Example results are shown in Figure 2.5. They indicate the effect of the cube mass on the pressure transients; they also show that the pressure at the top face is negligible in comparison to the pressure at the bottom face. The same holds for the pressures acting on the side faces.

In order to confirm the pressure evaluation the center-of-mass velocity v_{ave} of a cube is taken from the Lagrange part of the computation and differentiated with respect to time t . Multiplication with the factor m/A (mass of the cube divided by the bottom area) yields the average net pressure p_{ave} acting on the cube in the radial direction:

$$p_{ave} = \frac{m}{A} \frac{d}{dt} v_{ave} \quad .$$

Figure 2.6 shows a comparison between this average net pressure and the pressure difference acting on the cube bottom and top faces obtained from the Eulerian flow fields. It can be seen that for both tungsten and aluminum the two curves coincide well. This result is a good verification for the chosen method to determine the correct boundary conditions for the accelerated cubes in the launch phase.

The results obtained with the two-dimensional fluid-structure-coupled approach are summarized in Figure 2.7 in non-logarithmic and in logarithmic scale. It is evident that the pressure loads are highest for the pure tungsten cube and lowest for the pure aluminum cube. The mixtures fall consistently between these two curves.

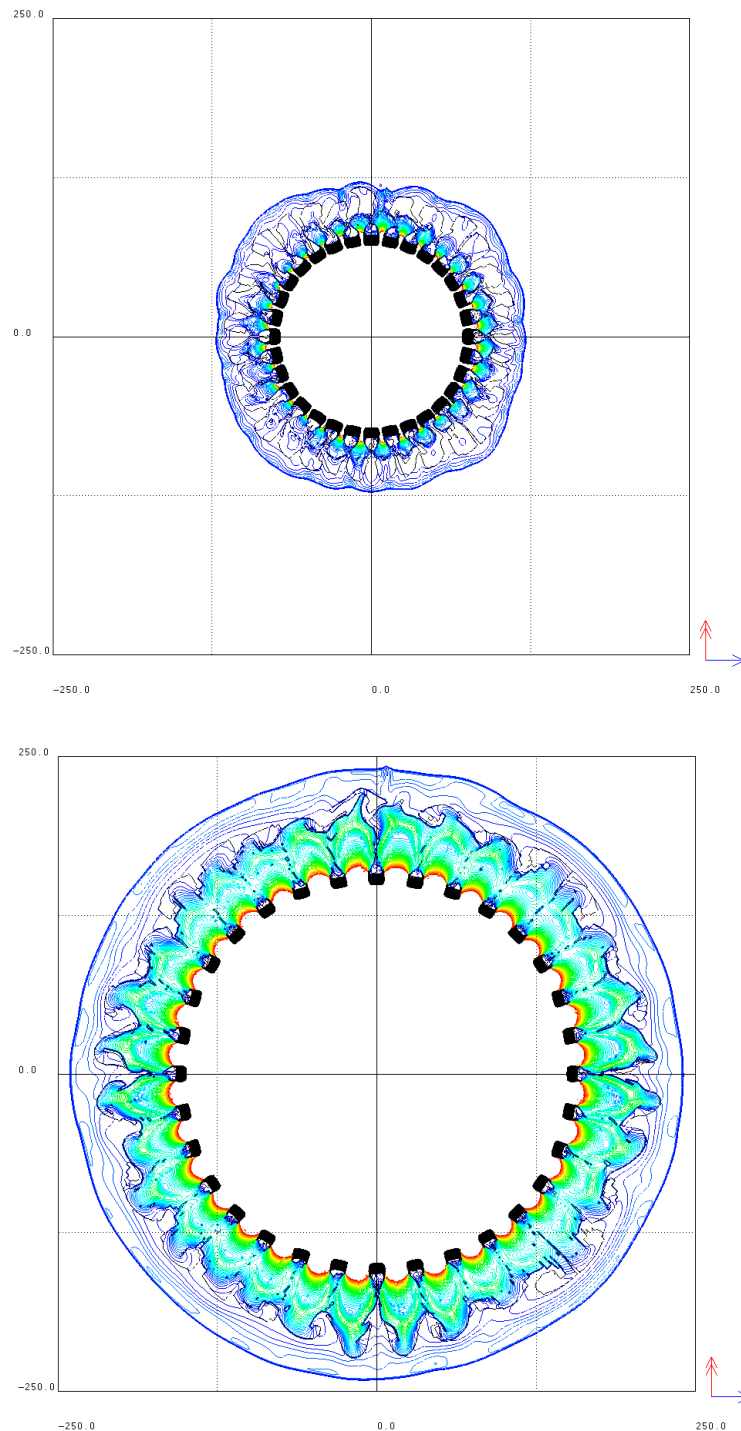


Figure 2.2: Density field at $t = 20 \mu\text{s}$ (above) and $t = 60 \mu\text{s}$ (below) after initiation of the TNT cylinder.

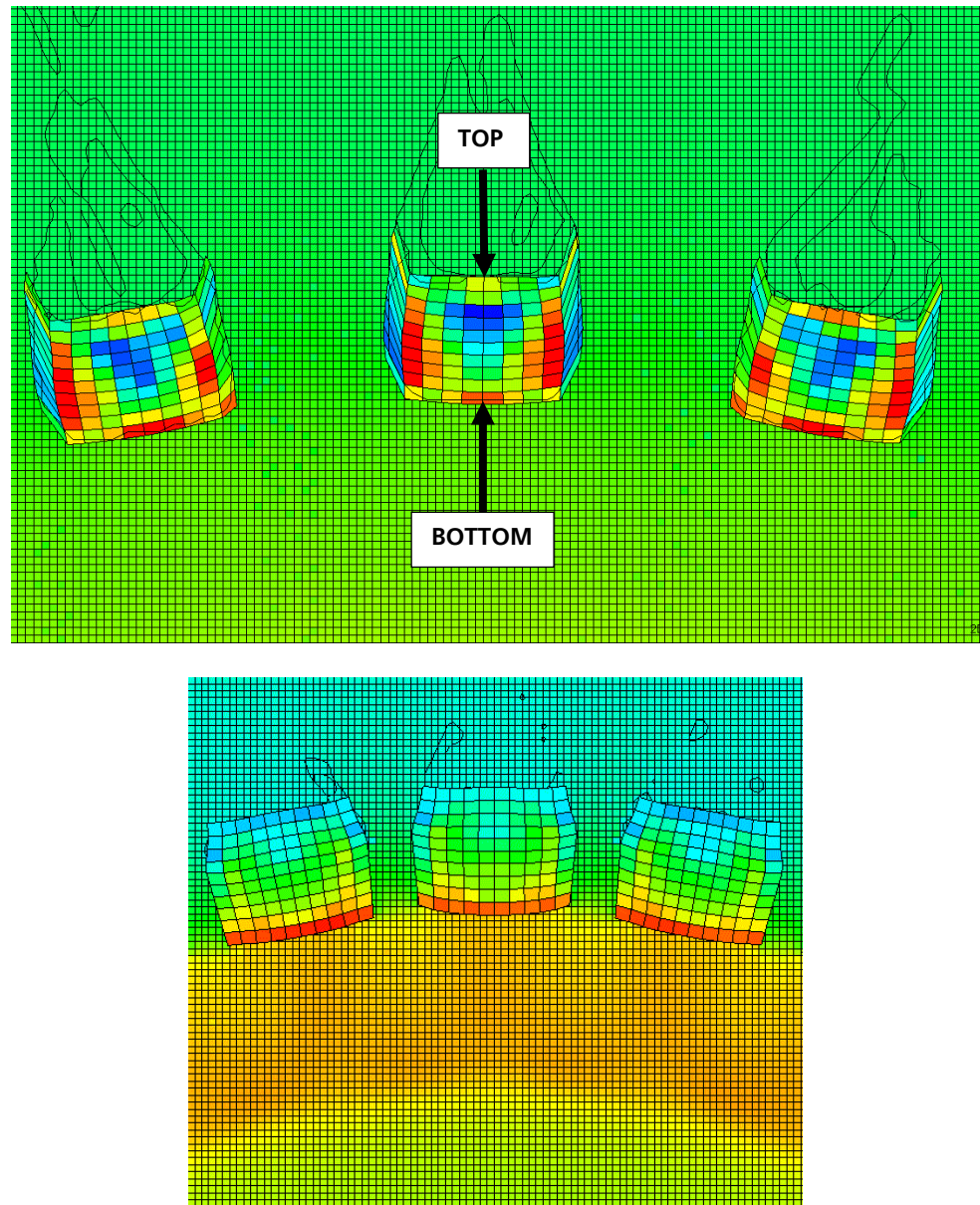


Figure 2.3: Enlarged view of aluminum cubes (above) and tungsten cubes (below) in the Eulerian mesh 40 μ s after initiation. The colors represent the pressure; red: high pressure, blue: low pressure.

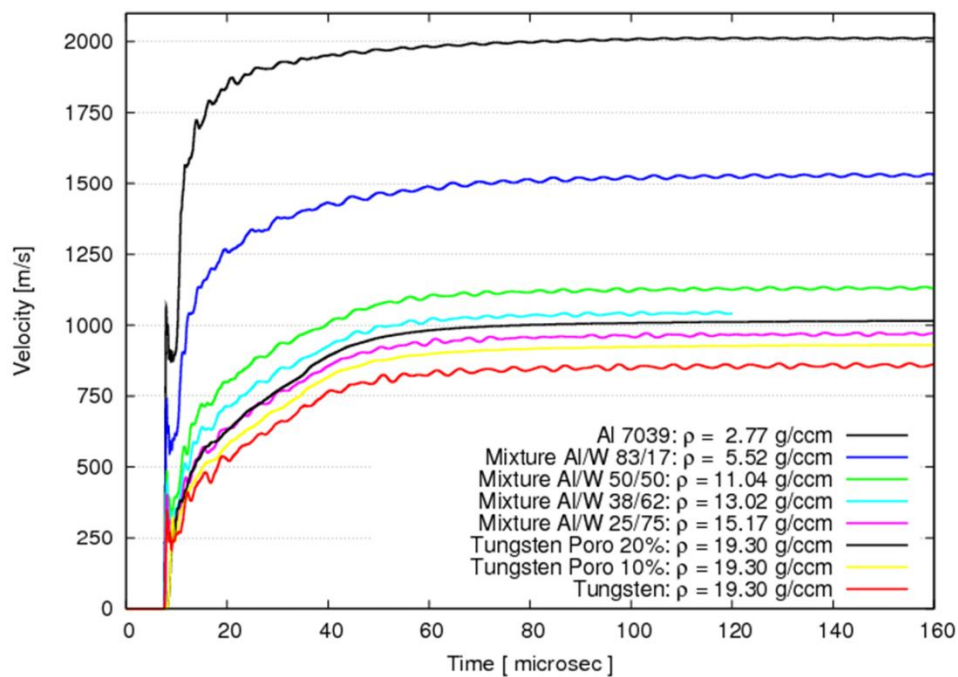


Figure 2.4: Absolute velocities of the cubes during launch phase: Al 7039, tungsten W, Al/W 83/17, Al/W 50/50, Al/W 38/62 and Al/W 25/75 and two tungsten cubes with 10 % and 20 % porosity. The end of the acceleration or launch phase is reached at about $t = 100 \mu\text{s}$.

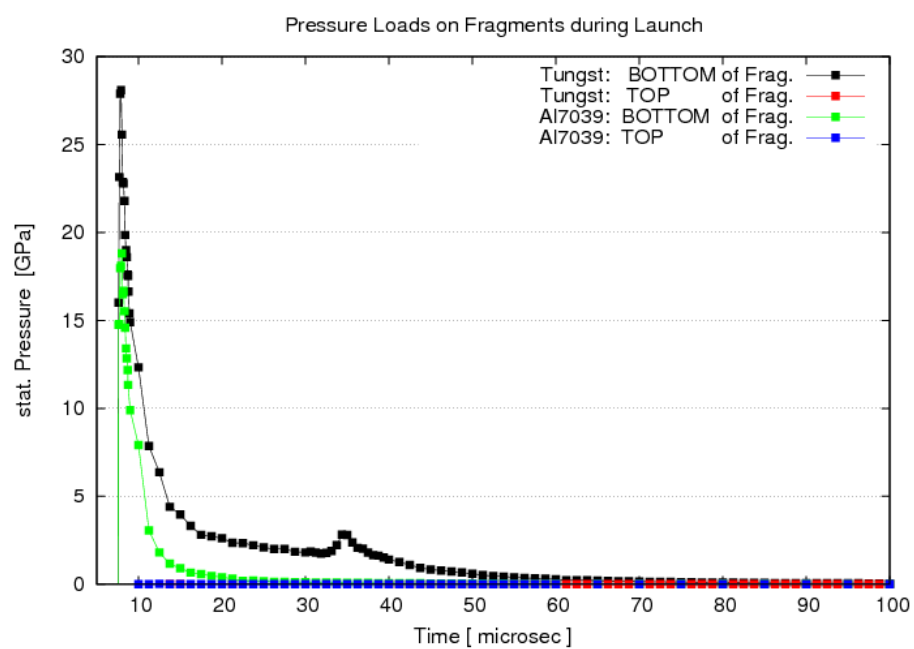


Figure 2.5: Pressure histories at the TOP and BOTTOM gauges of the cube in the Eulerian mesh.

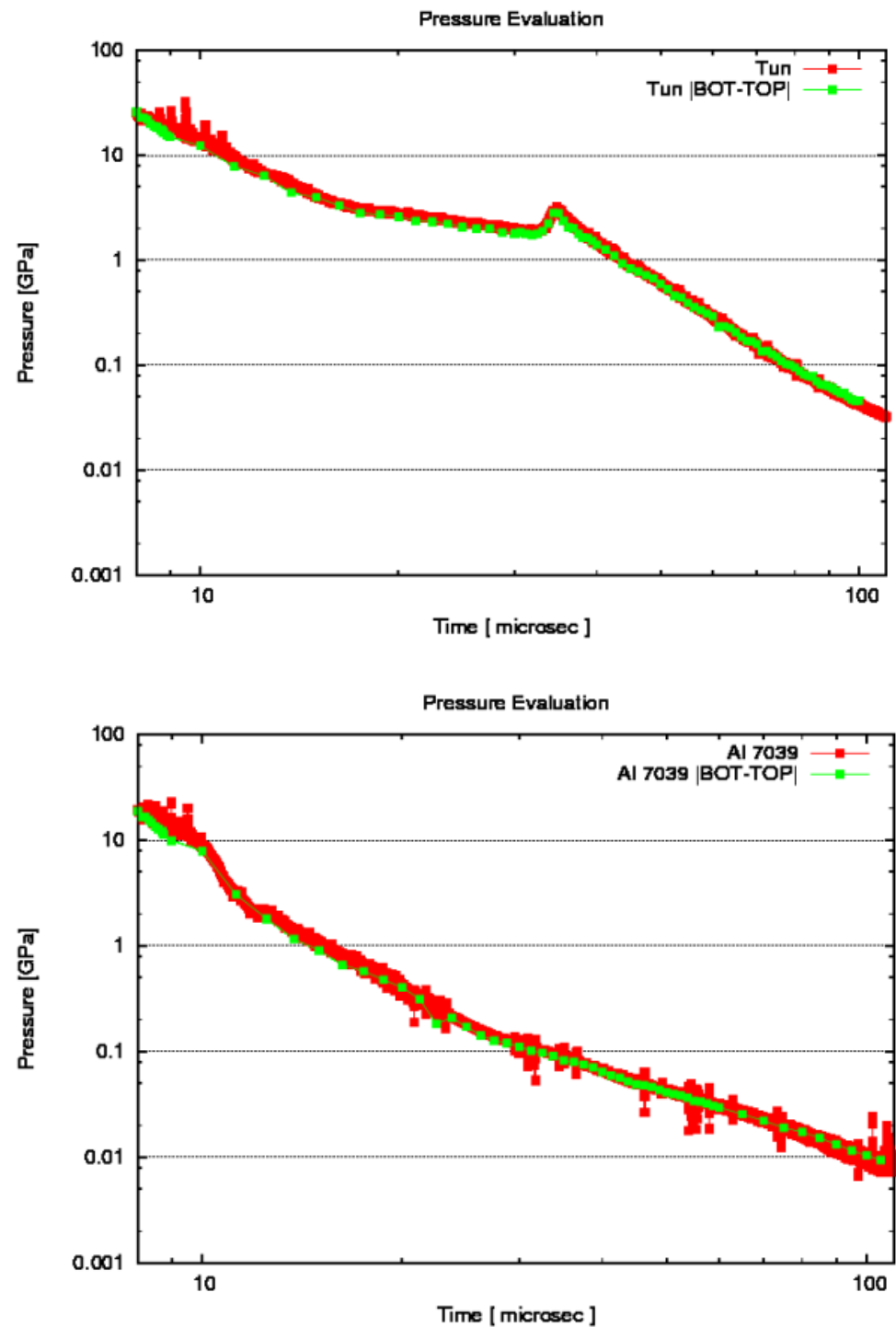


Figure 2.6: Average net pressures from the center-of-mass acceleration (red) and pressure difference between bottom and top face of a cube from moving gauges in the Euler mesh (green) for tungsten (upper diagram) and for aluminum (lower diagram).

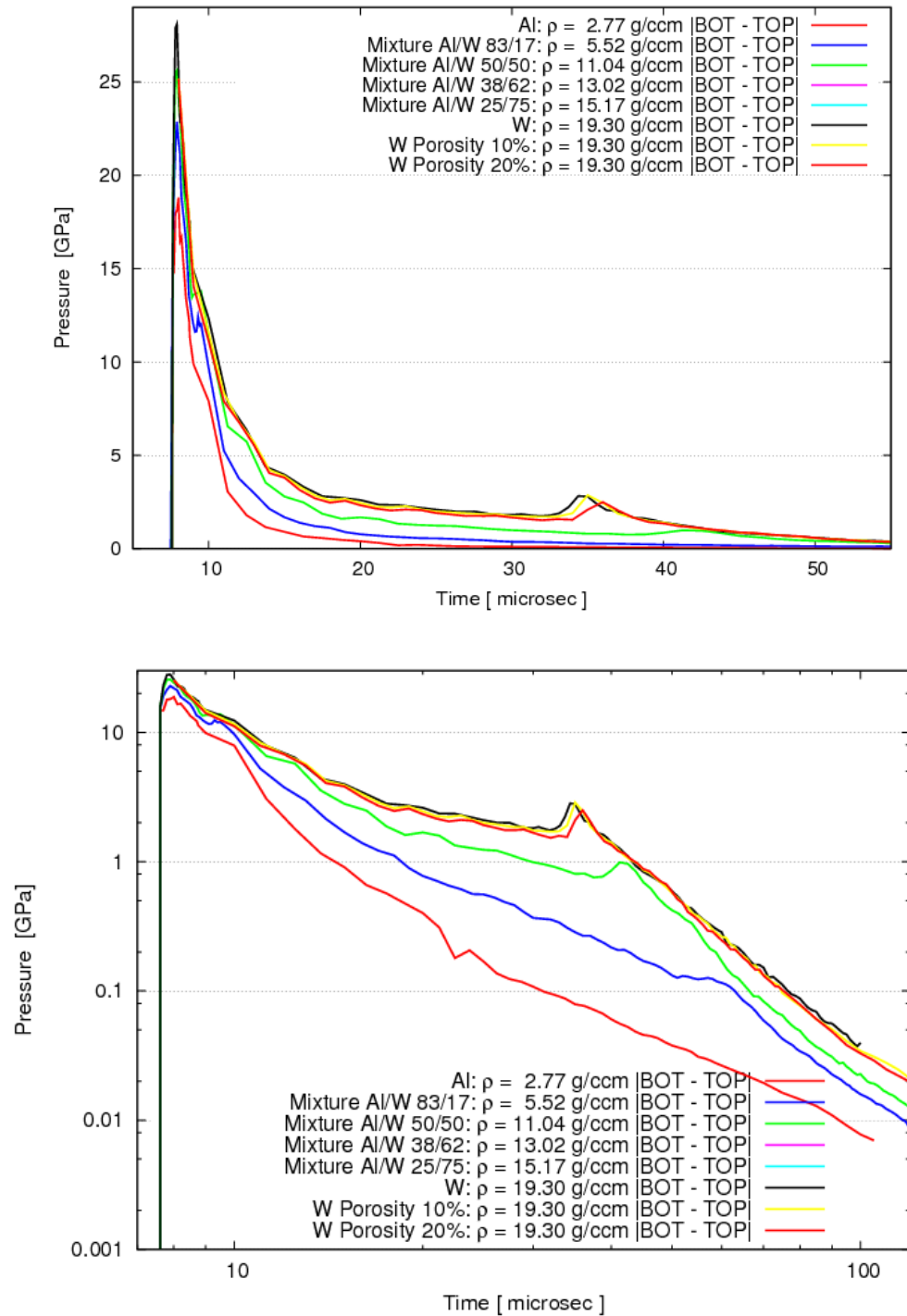


Figure 2.7: Resulting pressures (BOTTOM of the cube minus TOP of the cube) acting on the various cubes in non-logarithmic (above) and in logarithmic scale (below).

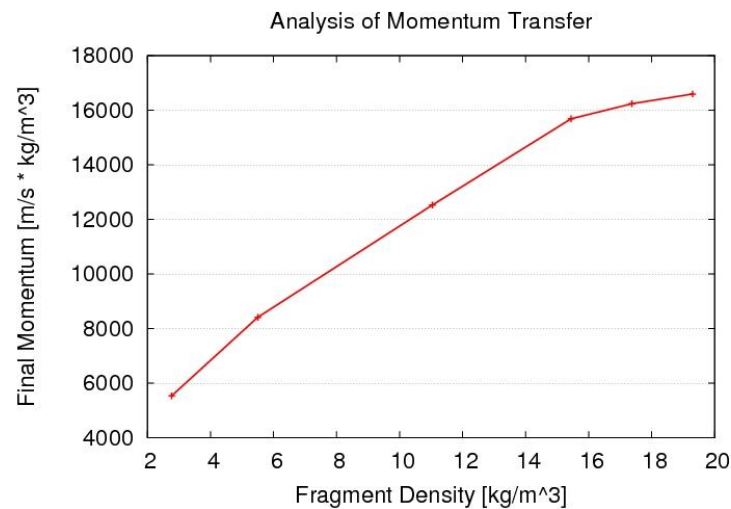


Figure 2.8: Total momentum transfer to the pre-fabricated fragments (cubes with 1 cm edge lengths) places onto cylindrical TNT charge with radius 52 mm.

Figure 2.8 summarizes the effect of the material density on the total momentum transfer for the investigated configuration. An important observation for the mesoscale simulations of the launch process is depicted in Figure 2.9. It shows that due to elastic-plastic deformation, the individual cubes stay in contact during the initial phase of the launch process. Thereby, they partly seal the gas volume during this time interval and also limit their further lateral deformation through their mutual lateral support.

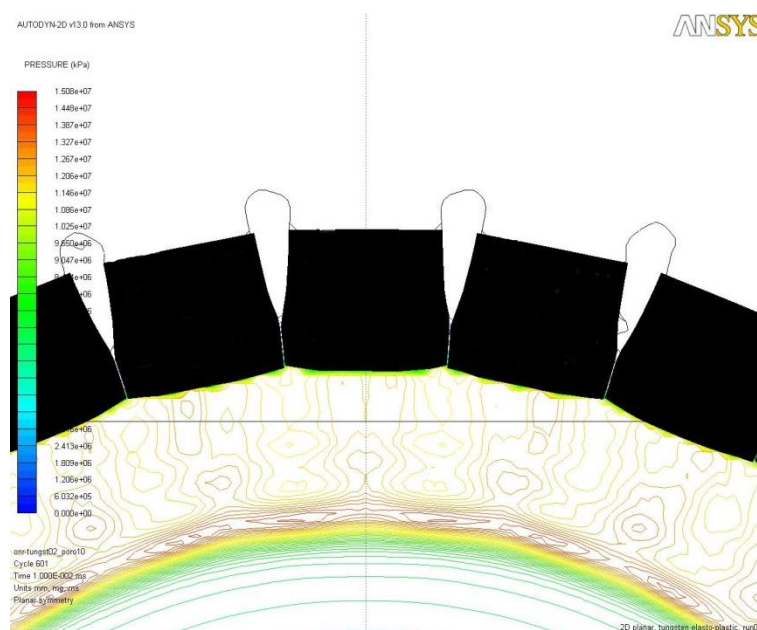


Fig. 2.9: Contact of adjacent cubes throughout extended time interval due to deformation (example for tungsten cubes).

2.4 Results of 3-D Simulations

In order to check the applicability of the two-dimensional simplification, an equivalent 3-D simulation has been performed for a selected case.

Figure 2.10 shows the corresponding numerical model in three dimensions. It consists of one Eulerian part (dark blue represents air) and in total 306 Lagrangian parts (red) for the metallic cubes, which are concentrically placed in a radius of 52.5 mm around the TNT cylinder (green). The Eulerian part has the dimensions 300 mm, 150 mm, 300 mm in xyz-direction and is built up with $200 \times 100 \times 200 = 2$ million elements. The cubes have 10 mm edge length and a spatial resolution of 2 mm (125 elements). The initiation point is on the face center of the cylinder.

The lower picture in Figure 2.10 shows the computed pressure field at the surfaces of the Eulerian part and the accelerated cubes (light blue) $40 \mu\text{s}$ after the initiation of the TNT cylinder. Each of the 17 circular layers of fragments is accelerated differently as the detonation propagates axially through the TNT cylinder.

The velocity of a cube located at half length of the cylinder has been evaluated and compared to the velocity obtained from the 2-D model, see Figure 2.11. In the 2-D computations the final velocities of the aluminum and the tungsten cubes (red curves) are about 10 % higher than the final velocities in the 3-D computations (black curves). This is due to the different geometry of the detonation wave in three dimensions and the possibility of the cubes to separate in the axial direction. Note that the movement of the fragments in the 3-D computation starts later than that of the 2-D computation. This results from the greater distance between the evaluated cube and the detonation initiation point.

The relatively small differences between the 2-D and the 3-D results indicate that the loading on the cubes during the explosive launch can be evaluated reasonably well from the 2-D computations.

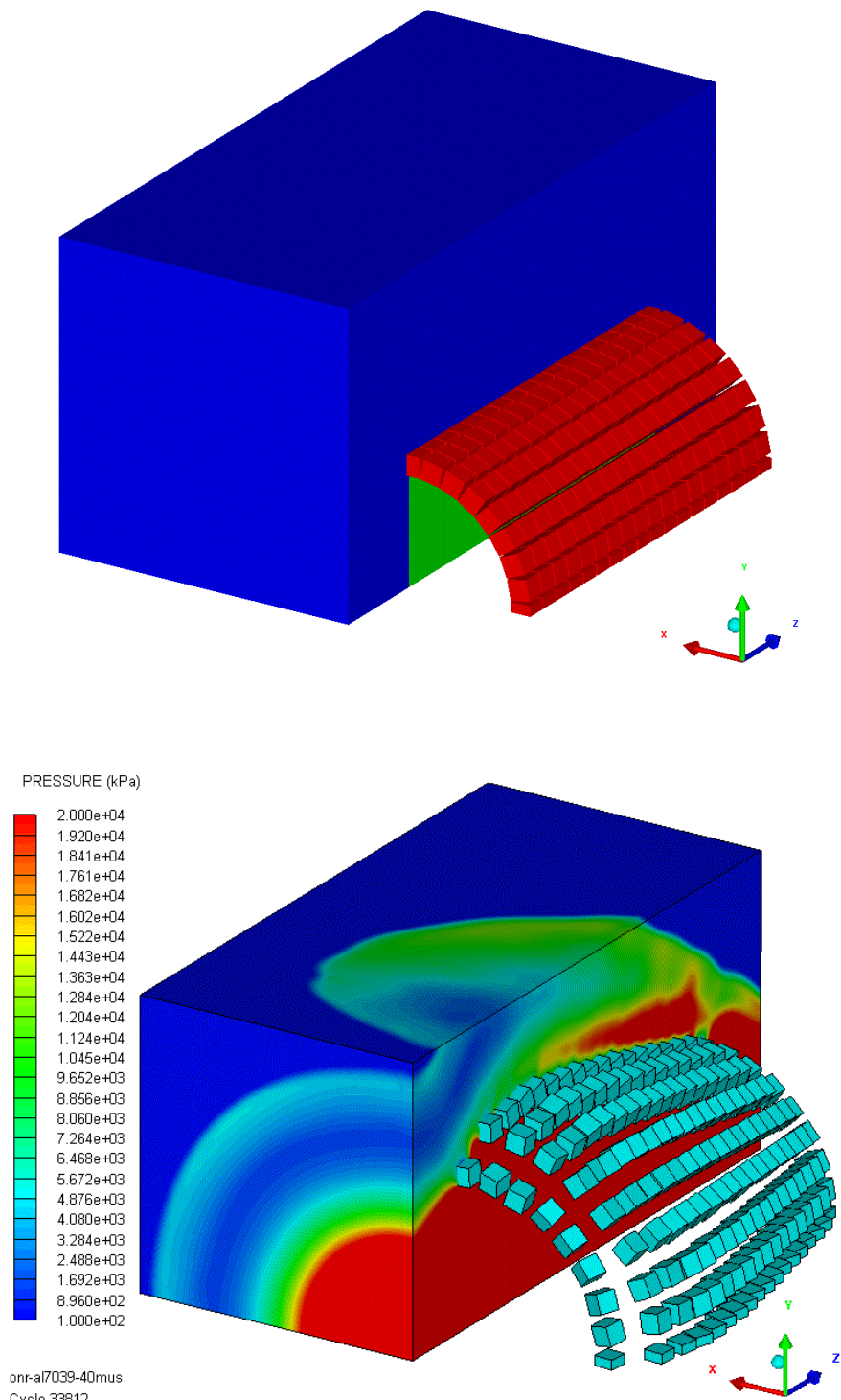


Figure 2.10: Top: 3-D Model; the $y=0$ plane is the symmetry plane of the model, the right half of the Euler mesh (dark blue) is hidden to display the arrangement of the fragments (red) and the TNT cylinder (green). Bottom: Computed pressures in the Euler part and positions of the fragments 40 μ s after initiation.

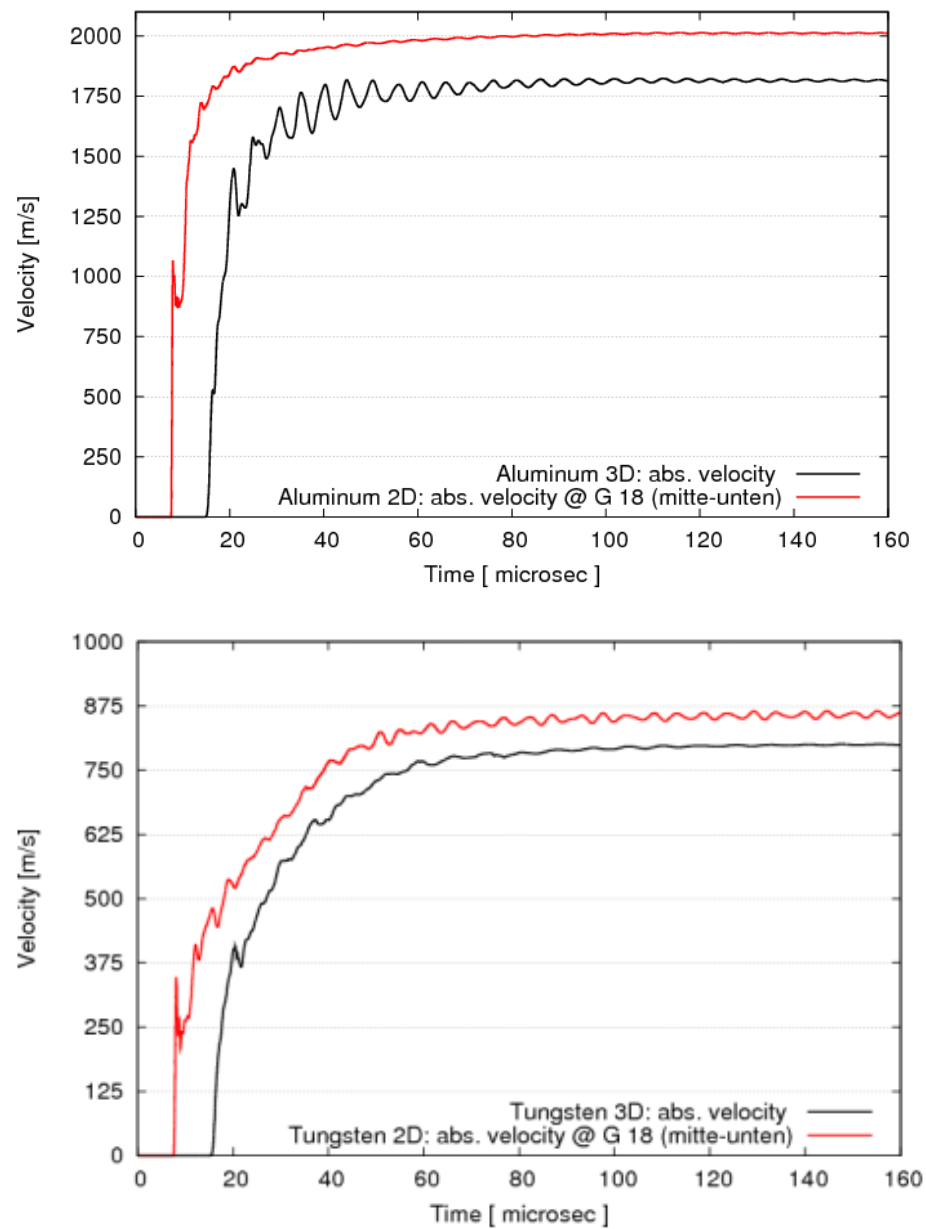


Figure 2.11: Comparison of the absolute velocities of the cubes in the 2-D simulation (red curves) and the 3-D simulation (black curves).

3 Mesoscale Material Modeling

3.1 Mesoscale Material Structures

The mesoscale material structures investigated in this project shall represent granular metallic structures produced by cold-pressing and sintering. The computational models are generated with GEOSTAT, [1], which produces voxel models of isotropic microstructures with user defined parameters for the mass fraction of constituent materials, the grain size distribution for each constituent and the overall porosity.

The algorithm in GEOSTAT places spheres with a user defined size distribution randomly into a cubic volume such that initially no overlapping occurs (Figure 3.1, left). This is followed by a growth phase which serves to adjust the porosity. In this phase the spheres are mapped onto a user-defined Cartesian grid, which defines the resolution of the voxel model (Figure 3.1, right). If two or more spheres are present in the same cell, the sphere with the highest cell volume fraction will be attributed to the entire cell. The growth phase continues until the desired porosity is reached. During the growth phase the mass fractions and grain size distributions are not conserved. The desired values of these parameters must therefore be adjusted iteratively by variation of the properties of the initially distributed spheres.

After generation of a RVE with GEOSTAT, grain boundaries were inserted. This was achieved by assigning designated material properties (grain border material) to one layer of elements on either side of the grain boundaries, see [1] for details.

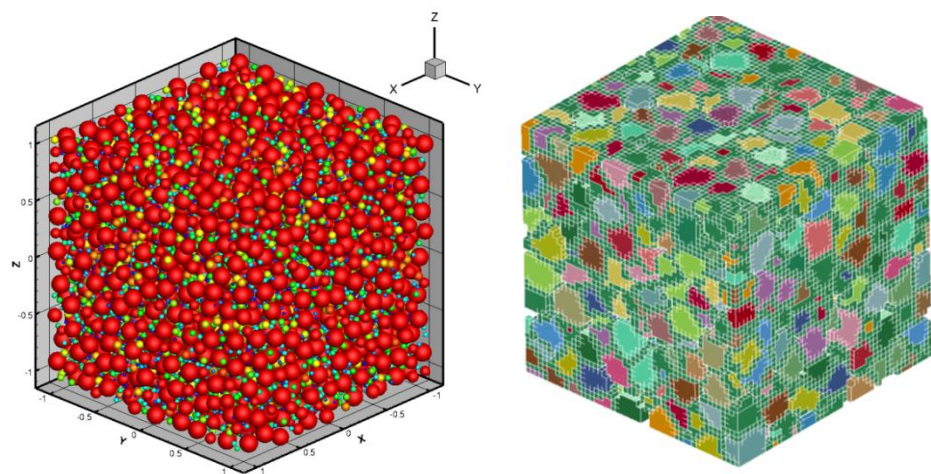


Figure 3.1: Left: Initial distribution of spheres (colors indicate sphere size). Right: Cartesian mesh of the resulting RVE (colors indicate individual grains).

In total 24 different RVEs have been generated by variation of the mass fractions, the grain size distributions and the porosities, as listed in Table 3.1.

In accordance with the applied macroscopic scaling (see Chapter 3.3) the edge lengths of the generated RVEs were 0.3 mm for the majority of cases. For selected cases, RVEs with larger dimensions (0.6 mm, 0.9 mm) were produced.

Table 3.1: Microstructural parameters of generated RVEs (composition given in volume fraction).

Material composition	W	Al/W 25/75	Al/W 38/62	Al/W 50/50	Al/W 83/17	Al
Nominal grain size distribution	Uniform: $D = 30 \mu\text{m}$			Non-uniform: $D = [7.5 \mu\text{m}, 45 \mu\text{m}]$		
Porosity	10 %			20 %		

The following figures present the grain size statistics in terms of cumulated grain numbers fractions for a few representative RVEs. Figure 3.2 (top) shows the cases with nominally “non-uniform” distributions for pure Al (the RVE is identical with that of pure W) and two mixtures; for each the cases with porosities 10 % and 20 % are included in the diagram. It can be seen that the grain size is roughly uniformly distributed within a range between about $10 \mu\text{m}$ to about $55 \mu\text{m}$. The deviation from the nominally desired values stems from the growth phase in GEOSTAT which adjusts the porosity. As the exact grain sizes are of minor importance for this study, no iterative adjustment was performed in the process of RVE generation. Figure 3.2 (bottom) presents for the same examples the cases with nominally “uniform” distribution. In the process of porosity adjustment the grains actually take on a non-uniform size distribution – otherwise small porosities of 10 % or 20 % could not be reached. In Figure 3.3 the same RVEs are presented in terms of cumulated grain volume fractions.

For this study it is important to note that the two variants “uniform” and “non-uniform” have clearly distinguishable statistics in the grain size distributions.

Table 3.2: Approximate median values of grain sizes in terms of cumulated grain volume and cumulated grain numbers (in brackets) for the cases “uniform” and “non-uniform” and two porosities.

	10 % Porosity	20 % Porosity
“uniform”	39 μm (37 μm)	37 μm (36 μm)
“non-uniform”	45 μm (26 μm)	42 μm (22 μm)

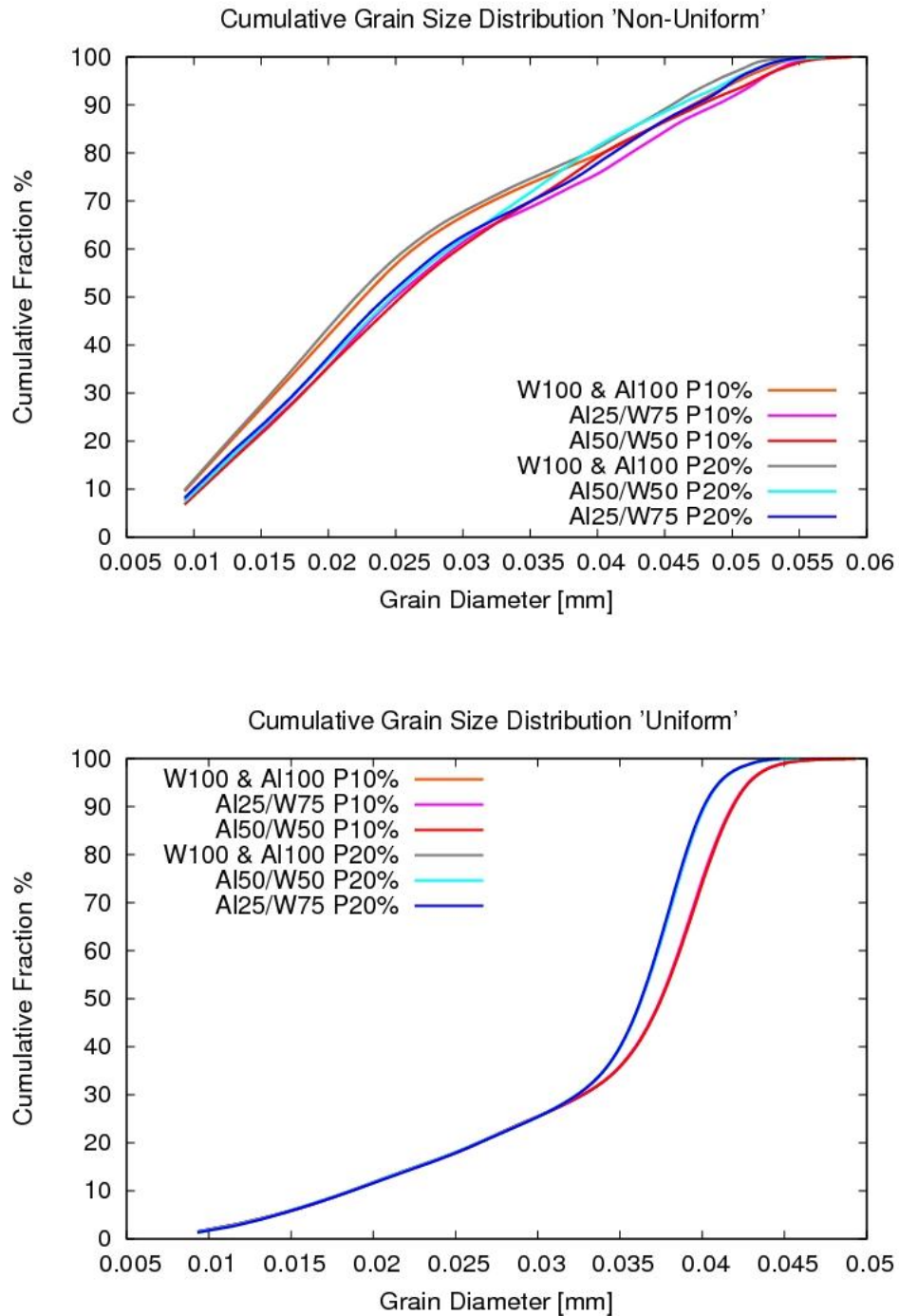


Figure 3.2: Grain size distributions for some cases with “uniform” distribution (top) and “non-uniform” distribution (bottom) in terms of grain number fractions.

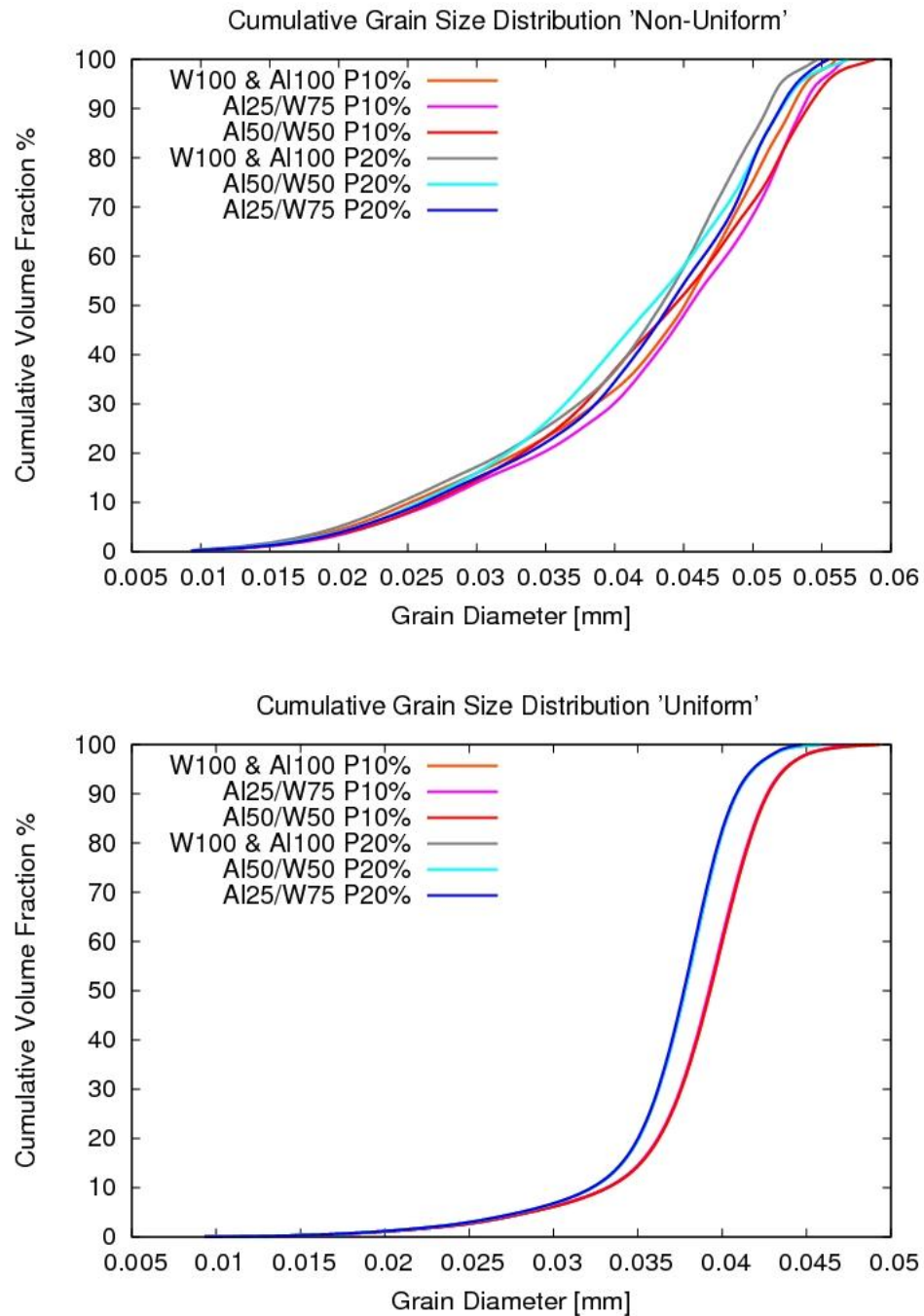


Figure 3.3: Grain size distributions for some cases with “uniform” distribution (top) and “non-uniform” distribution (bottom) in terms of grain volume fractions.

3.2 Computational Models and Material Properties

The LS-DYNA software has been used for all mesoscale simulations in this project. The computational model of the pre-formed cubic fragment with resolved microstructure is obtained from the voxel models described in the previous section. These voxel models provide hexahedral finite-element models. Granular failure was excluded; inter-granular failure was computationally treated with the node-split approach, as described further below.

The material modeling approach is identical with the one used in the previous project: isotropic elastic-plastic models have been applied for both grains and inter-granular border material. A linear equation of state and a simplified variant of the Johnson-Cook strength model, [9], have been used, where the yield stress is defined by

$$\sigma_Y = (\sigma_{Y0} + B \epsilon_{pl}^n).$$

The equation of state parameters and the parameters of the strength model are taken over from the models used in the macroscale simulations (Steinberg-Guinan model for tungsten and Al 7039, [8]).

As shown in [1], mesoscale simulations which include inter-granular fracture can predict to some extent the strain rate dependency of the macroscopic material strength. No additional strain rate effects or temperature dependencies were thus modeled on the mesoscale in this study.

The inter-granular border material is modeled with the same material parameters as the respective grains, except for the yield stress which is reduced by a factor α . This factor represents the ratio of inter-granular cohesive strength to bulk grain strength. As this ratio can be influenced by material production processes, e. g. by sintering temperature and pressure, different values have been considered in this study.

Inter-granular failure is modeled via the node-split approach. Upon fulfillment of a failure criterion for a node, the node is duplicated for each connected grain and the duplicated nodes are then permitted to separate from each other. This introduces an internal surface without the need to erode elements. As a failure criterion, the effective plastic strain in the adjacent grain elements (border elements) is chosen. As in the previous project, a statistical distribution of the failure strain has been introduced to achieve a better representation of a realistic hardening behavior. The failure strain values are distributed randomly in space with uniform statistical distributions from a chosen interval. Through this distribution the node-split process happens progressively within the RVE. The applied failure strain intervals are listed in Tables 3.3 to 3.5. They are specified individually for each inter-granular material combination.

A disadvantage of the current node-splitting approach results from the fact that it is not possible to discriminate between intra- and inter-granular pairs of nodes. Thus a node-splitting may affect up to eight elements, including those which are part of the same grain. This leads to short cracks in the direction normal to the grain interface, as can be recognized in Figure 3.4. However, this only happens at elements right on the grain border and we assume a minor effect on the overall results.

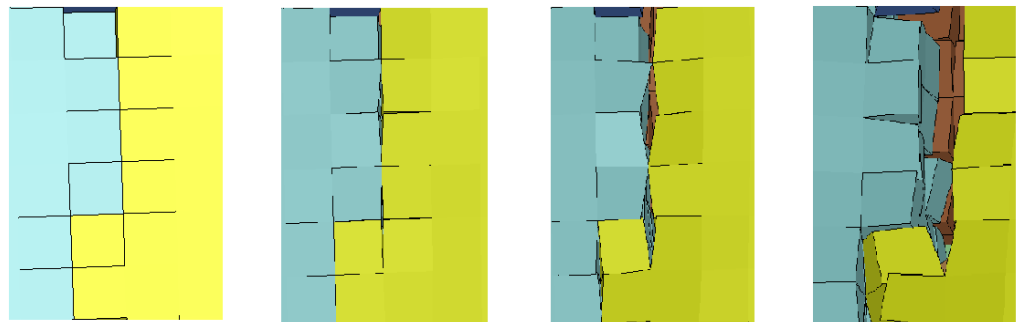


Figure 3.4: Progressive generation of cracks between two grains and normal to grain surfaces.

Table 3.3: Material data for tungsten.

Tungsten			
RVE edge length and resolution	L = 0.3 mm n = 40 ³ elements	L = 0.6 mm n = 80 ³ elements	L = 0.9 mm n = 120 ³ elements
Grain distribution	Uniform: D = 30 μm		Non-uniform: D = [7.5 μm , 45 μm]
Porosity	10 %		20 %
Material data of grains and border	$\rho = 19.3 \text{ g/cm}^3$ G = 160 GPa K = 313 GPa B = 1.055 GPa n = 0.82		
Yield stress of grains	$\sigma_{Y0}^{\text{grains}} = 2.2 \text{ GPa}$		
Yield stress of border	Strong border ($\alpha = 80 \%$): $\sigma_{Y0} = 1.76 \text{ GPa}$		Weak border ($\alpha = 30 \%$): $\sigma_{Y0} = 0.66 \text{ GPa}$
Failure strain interval of border	[0.05, 0.15]	[0.10, 0.30]	[0.20, 0.40]

Table 3.4: Material data for aluminum.

Aluminum					
RVE edge length and resolution	L = 0.3 mm n = 40 ³ elements		L = 0.6 mm n = 80 ³ elements		L = 0.9 mm n = 120 ³ elements
Grain distribution	Uniform: D = 30 μm			Non-uniform: D = [7.5 μm , 45 μm]	
Porosity	10 %			20 %	
Material data of grains and border	$\rho = 2.76 \text{ g/cm}^3$ G = 25.8 GPa K = 78.5 GPa B = 0.36 GPa n = 0.34				
Yield stress of grains	$\sigma_{Y0}^{\text{grains}} = 0.2 \text{ GPa}$		$\sigma_{Y0}^{\text{grains}} = 0.4 \text{ GPa}$		$\sigma_{Y0}^{\text{grains}} = 0.8 \text{ GPa}$
Yield stress of border	Strong border ($\alpha = 80 \%$): $\sigma_{Y0}^{\text{border}} = 0.8 \sigma_{Y0}^{\text{grains}}$			Weak border ($\alpha = 30 \%$): $\sigma_{Y0}^{\text{border}} = 0.3 \sigma_{Y0}^{\text{grains}}$	
Failure strain interval of border	[0.05, 0.15]	[0.1, 0.3]	[0.2, 0.4]	[0.3, 0.6]	[0.4, 0.8]

Table 3.5: Additional material data for Al/W mixtures.

Al/W Mixtures	
Yield stress of Al/W border	$\sigma_{Y0}^{\text{border}} = 0.2 \text{ GPa}$
Failure strain interval of Al/W border	[0.05, 0.15]

3.3 Geometrical Scaling on the Macroscale

The pre-formed cubic fragments considered in this investigation have an edge length of 1 cm and are composed of grains with an average size of about 30–40 μm . As the grains need to be adequately resolved in the mesoscale computation, an edge length of finite elements of about 3–4 μm is required. Therefore, roughly 20–40 billion elements would be needed to discretize the entire cube. This is beyond the computational capabilities normally available today. To overcome this limitation, geometrical scaling was applied to the macroscale.

In the applied approach, all macroscopic geometric dimensions are scaled down, velocities and material parameters expressed in terms of stresses and pressures remain unchanged (see Table 3.6).

The geometrical scaling is applied only for the outer dimensions of the cube and the target plate. The granular structure (e. g. grain size distribution) remains at true scale. The result is a smaller cube with fewer grains, which can be computationally analyzed with the available resources.

The majority of the presented results have been obtained for scaling ratios of 1:33, i.e. the downscaled cubes had an edge length of 0.3 mm. The validity of the scaling approach was further investigated by performing analyses with larger scales (edge lengths of 0.6 and 0.9 mm), see Chapter 7 for details.

Table 3.6: Geometrical scaling with scaling factor λ and resulting scaling rules for selected derived quantities.

Basic quantities	Symbol	Dimension	Scaling
Length	L	L	$\lambda \cdot L$
Mass	M	M	$\lambda^3 \cdot M$
Time	t	t	$\lambda \cdot t$
Temperature	T	T	T
Derived quantities			
Velocity	v	L / t	v
Acceleration	a	L / t^2	a / λ
Density	ρ	M / V^3	ρ
Force	F	$M \cdot L / t^2$	$\lambda^2 \cdot F$
Energy	E	$M \cdot L^2 / t^2$	$\lambda^3 \cdot E$
Pressure, stress	p, σ	$M / (L \cdot t^2)$	p, σ
Strain	ε	L / L	ε
Strain rate	$\dot{\varepsilon}$	$L / (L \cdot t)$	$\dot{\varepsilon} / \lambda$

3.4 Fragment Size Analysis

In order to determine a quantitative measure for the fragment sizes observed in the simulations, a suitable evaluation method has been applied. The evaluation is based on the LS-PREPOST output file (LS-PREPOST is the standard postprocessing tool for LS-DYNA), which comprises the entire mesh information, i.e. the element inventory with their respective attributed nodes at a specific timestep. With this information, it is possible to identify individual fragments in the model. A small software routine has been developed to identify these fragments and sort them into volume or mass bins.

Figure 3.5 illustrates an undesired side-effect of the node-splitting approach. Due to the short cracks that can occur normal to grain surfaces, it may happen that grains are fragmented, as single protruding elements are cut off from a grain. Such cases are recognized in the statistical evaluation by checking the grain IDs of the

fragments. The artificial fragments of one grain are then evaluated as one single grain.

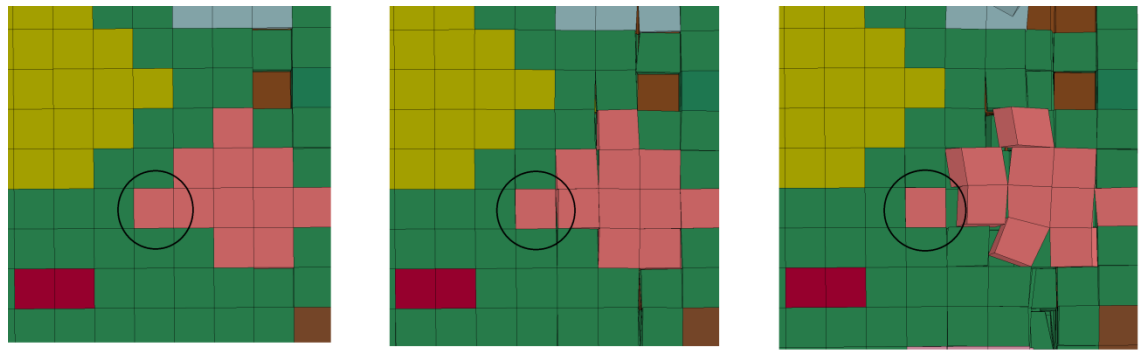


Figure 3.5: Node-split might lead to artificial fracturing of grains. These fractures are not considered in the evaluation of fragment size distributions.

As a characteristic measure of the fragment size distribution, we evaluated the median fragment size with respect to the cumulated fragment volumes. These median sizes can be compared to the median grain sizes given in Table 3.2) to permit an easy assessment of the degree of fragmentation.

Note that fragment and grain sizes are given in terms of the diameter of volume equivalent spheres.

4 Mesoscale Launch Simulations and Analysis

4.1 Launch Modeling

The macroscale launch simulations presented in Chapter 2 provided the transient fluid pressures which act on the faces of a pre-formed cubic fragment. To impose these launch conditions on the cube in the mesoscale simulations, the local pressure transients at representative points were smoothly interpolated on the external faces of the cube as sketched in the following figure.

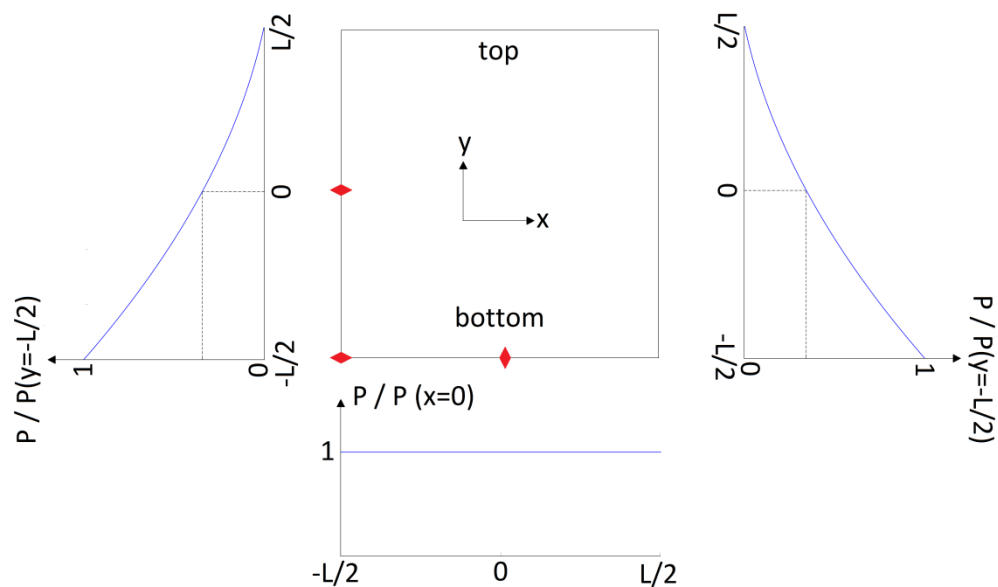


Figure 4.1: Schematic representation of the pressure profiles acting on the faces of the cube. Pressures are interpolated between values at representative points (red marks) obtained from gauges in the macroscale launch simulations.

This pressure distribution is applied as time-dependent boundary condition for the cube using a scaled time. The cube size (RVE edge length) used in the simulations presented in this chapter was 0.3 mm (original cubed size is 1 cm), i.e. a scaling of about 1:33 was applied. The same scaling was used for the time dependency of the pressure loads.

Contrary to the macroscale launch simulations, in which all cubes surrounding the explosive charge are modeled, only one cube is considered in the mesoscale simulations. The lateral support by adjacent cubes which occurs due to cube deformation during the initial acceleration phase (c.f. Figure 2.9) must therefore be adequately modeled. This is achieved by inserting symmetry planes around the cube as shown in Figure 4.2. By means of these symmetry planes, the cube is constrained

to move within a rigid funnel, which models the initial lateral support of the adjacent cubes.

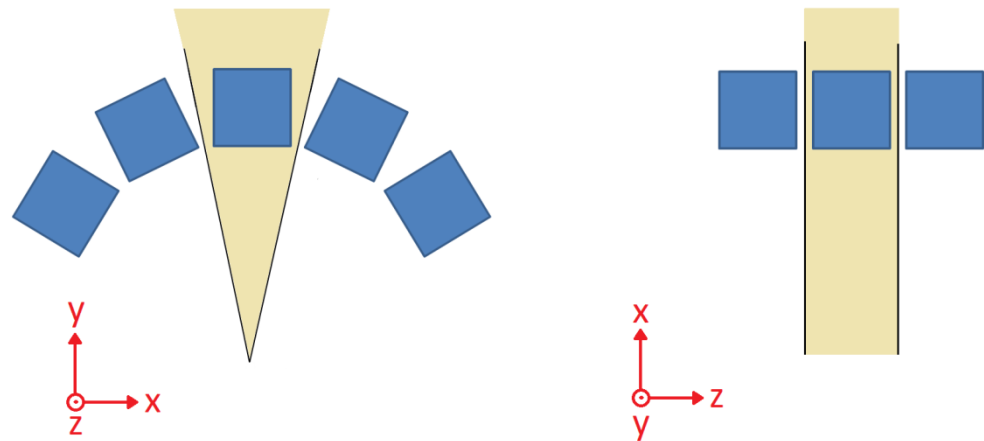


Figure 4.2: Definition of rigid surfaces around the simulated cube to model the contact between adjacent cubes due to deformation during the launch process. Left: view in the axial direction. Right: view in the radial direction.

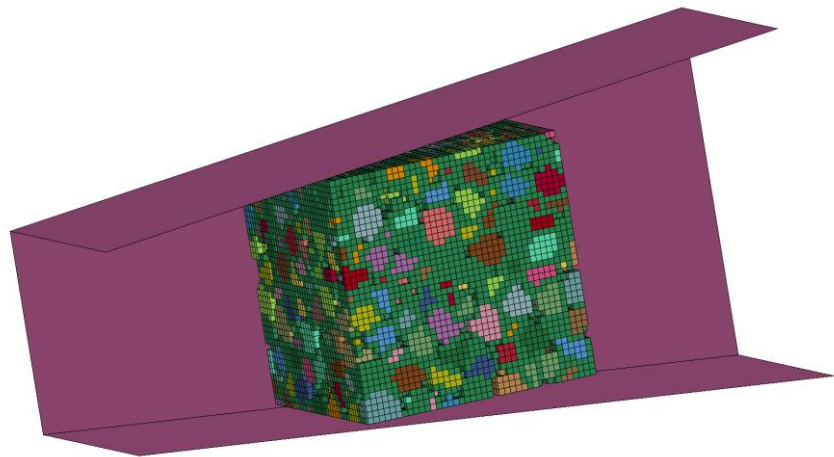


Figure 4.3: Downscaled cube surrounded by the rigid surfaces schematically shown in Figure 4.2.

4.2 Launch Simulation Results

The numerical model for the launch simulations is shown in Figure 4.3. Due to the applied transient pressures, the cube is accelerated out of the funnel in x-direction. At a scaled time of $3 \mu\text{s}$ ($100 \mu\text{s}$ in the original scale), the RVE has reached its final velocity and its state can be evaluated.

The two materials initially investigated were pure tungsten and pure aluminum, each with the stronger variant of the inter-granular border (1.76 GPa for tungsten and 0.16 GPa for aluminum). The varied parameters were the grain size distribution

(uniform or non-uniform), the porosity (10 % porosity or 20 % porosity) and the failure strain distribution (ranging from 0.05 to 0.8). For the aluminum RVEs also the yield stress of the grains was varied.

Figure 4.4 shows a typical result for the tungsten RVEs at time 3.0 μ s. At the left side, one can see the end of the funnel. On the right side, the compressed but almost intact tungsten cube can be seen. Only a few small fragments can be observed in its surrounding.

For the aluminum cubes, the results are different. Figures 4.5 and 4.6 show two typical results, in which the aluminum cubes fragment to a large degree. The two cubes shown differ in the failure strain interval and in the yield stress of the grains. The case shown in Figure 4.6 had a yield stress of 0.8 GPa, which is well beyond normal aluminum strength. Even for this hypothetically strong material, the cube can be described as totally damaged; nevertheless the agglomeration of the fragments is more compact as in Figure 4.5, where the aluminum grains are modeled with a (more realistic) yield stress of 0.2 GPa. In fact, both aluminum cubes do not survive the high acceleration in the simulated launch process.

Based on these findings, a systematic study of the behavior of aluminum and tungsten mixtures was performed. The results are given in detail in the following Tables 4.1 to 4.6.

In summary, the tungsten cubes show considerable deformation but survive the launch, even with low inter-granular failure strains. Grain size distribution and porosities do not significantly affect the results. This is due to the high strength and density of the tungsten grains and the relatively high strength of the inter-granular boundary. At lower inter-granular strength values the porosity and further parameters start to influence the results. However, only the case with porosity 20 % and the "uniform" grain size distribution shows considerable damage. This finding is also illustrated in Figures 4.15 to 4.18, which show the accelerated scaled tungsten RVEs after 3 μ s.

None of the pure aluminum RVEs survived the launch (Table 4.6 and Figures 4.5 to 4.8).

For the mixtures, only specific variants with a low aluminum content of 25 % (volume) seem capable to withstand the loading (Table 4.2 and Figures 4.9 to 4.12). These are the variants with 10 % porosity and high inter-granular strength. In particular, the case with "non-uniform" grain size distribution seems to perform best.

All other investigated composites with higher aluminum content, i.e. 38 %, 50 % and 83 %, are seriously damaged during launch, such that their penetration capability at larger distances would be drastically reduced (Tables 4.3 to 4.4 and Figures 4.13 and 4.14). These results are also reflected in the analysis of the average fragment size in Figure 4.19.



Figure 4.4: Non-uniform tungsten RVE with porosity 10 % and yield stress 0.66 GPa.



Figure 4.5: Non-uniform aluminum RVE with porosity 10 % and yield stress 0.2 GPa.

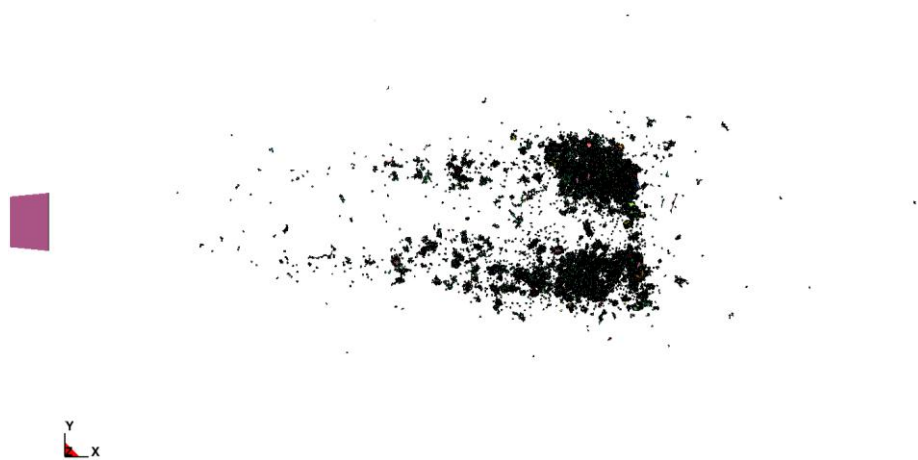


Figure 4.6: Non-uniform aluminum RVE with porosity 10 % and yield stress 0.8 GPa.

Table 4.1: Summary for the launch simulations with Tungsten. The final time is $t_{\max} = 3 \mu\text{s}$.

Mat.	Grain size distribution	Porosity [%]	Grain boundary strength [GPa]	Failure strain interval	Results		
					Damage state at t_{\max}	Velocity (t_{\max}) [m/s]	Displacement (t_{\max}) [mm]
W	Non-uniform	10	1.76	0.05 to 0.15	Intact, few fragments	1068.69	2.486
W	Non-uniform	20	1.76	0.10 to 0.30	Intact, few fragments	1100.56	2.554
W	Non-uniform	10	0.66	0.20 to 0.40	Intact, few fragments	1096.71	2.541
W	Non-uniform	20	0.66	0.05 to 0.15	Intact, few fragments	1104.12	2.557
W	Uniform	10	1.76	0.05 to 0.15	Intact, few fragments	1042.78	2.423
W	Uniform	20	1.76	0.05 to 0.15	Intact, few fragments	1075.67	2.487
W	Uniform	10	0.66	0.05 to 0.15	Intact, few fragments	1070.62	2.477
W	Uniform	20	0.66	0.05 to 0.15	Damaged	1067.15	2.461

Table 4.2: Summary for the launch simulations with Al25/W75. The final scaled time is $t_{\max} = 3 \mu\text{s}$.

Mat.	Grain size distribution	Porosity [%]	Grain boundary strength Al/W [GPa]	Failure strain interval	Yield stress of Al [GPa]	Results
						Damage state at t_{\max}
Al25/W75	Non-uniform	10	0.32/1.76	0.05 to 0.15	0.2	Intact, few fragments
Al25/W75	Non-uniform	20	0.32/1.76	0.05 to 0.15	0.2	Totally damaged
Al25/W75	Non-uniform	10	0.32/0.66	0.05 to 0.15	0.2	Almost intact, few fragments
Al25/W75	Non-uniform	20	0.32/0.66	0.05 to 0.15	0.2	Seriously damaged
Al25/W75	Uniform	10	0.32/1.76	0.05 to 0.15	0.2	Intact, few fragments
Al25/W75	Uniform	20	0.32/1.76	0.05 to 0.15	0.2	Totally damaged
Al25/W75	Uniform	10	0.32/0.66	0.05 to 0.15	0.2	Damaged
Al25/W75	Uniform	20	0.32/0.66	0.05 to 0.15	0.2	Totally damaged

Table 4.3: Summary for the launch simulations with Al38/W62. The final (scaled) time is $t_{\max} = 3 \mu\text{s}$.

Mat.	Grain size distribution	Porosity [%]	Grain boundary strength Al/W [GPa]	Failure strain interval	Yield stress of Al [GPa]	Results
						Damage state at t_{\max}
Al38/W62	Non-uniform	10	0.32/1.76	0.05 to 0.15	0.2	Damaged, less fragments
Al38/W62	Non-uniform	20	0.32/1.76	0.05 to 0.15	0.4	Seriously damaged
Al38/W62	Non-uniform	10	0.32/0.66	0.05 to 0.15	0.4	Seriously damaged
Al38/W62	Non-uniform	20	0.32/0.66	0.05 to 0.15	0.4	Totally damaged

Table 4.4: Summary for the launch simulations with Al50/W50. The final time is $t_{\max} = 3 \mu\text{s}$.

Mat.	Grain size distribution	Porosity [%]	Grain boundary strength [GPa]	Failure strain interval	Yield stress of Al [GPa]	Results
						Damage state at t_{\max}
Al50/W50	Non-uniform	10	0.32/1.76	0.05 to 0.15	0.2	Damaged, many fragments
Al50/W50	Non-uniform	20	0.32/1.76	0.05 to 0.15	0.2	Damaged, many fragments
Al50/W50	Non-uniform	10	0.32/0.66	0.05 to 0.15	0.2	Damaged, many fragments
Al50/W50	Non-uniform	20	0.32/0.66	0.05 to 0.15	0.2	Damaged, many fragments

Table 4.5: Summary for the launch simulations with Al83/W17. The final time is $t_{\max} = 3 \mu\text{s}$.

Mat.	Grain size distribution	Porosity [%]	Grain boundary strength [GPa]	Failure strain interval	Yield stress of Al [GPa]	Results
						Damage state at t_{\max}
Al83/W17	Non-uniform	10	0.32/1.76	0.05 to 0.15	0.2	Totally damaged
Al83/W17	Non-uniform	20	0.32/1.76	0.05 to 0.15	0.4	Totally damaged
Al83/W17	Non-uniform	10	0.32/0.66	0.05 to 0.15	0.4	Totally damaged
Al83/W17	Non-uniform	20	0.32/0.66	0.05 to 0.15	0.4	Totally damaged

Table 4.6: Summary for the launch simulations with Aluminum. The final scaled time is $t_{\max} = 3 \mu\text{s}$.

Mat.	Grain size distribution	Porosity [%]	Grain boundary strength [GPa]	Failure strain interval	Yield stress of Al [GPa]	Results
						Damage state at t_{\max}
Al	Non-uniform	10	0.16	0.05 to 0.15	0.2	Totally damaged
Al	Non-uniform	10	0.32	0.10 to 0.30	0.4	Totally damaged
Al	Non-uniform	10	0.32	0.20 to 0.40	0.4	Totally damaged
Al	Non-uniform	10	0.32	0.40 to 0.60	0.4	Totally damaged
Al	Non-uniform	10	0.32	0.60 to 0.80	0.4	Totally damaged
Al	Non-uniform	10	0.64	0.20 to 0.40	0.8	Totally damaged
Al	Non-uniform	20	0.16	0.05 to 0.15	0.2	Totally damaged
Al	Uniform	10	0.16	0.05 to 0.15	0.2	Totally damaged
Al	Uniform	20	0.16	0.05 to 0.15	0.2	Totally damaged

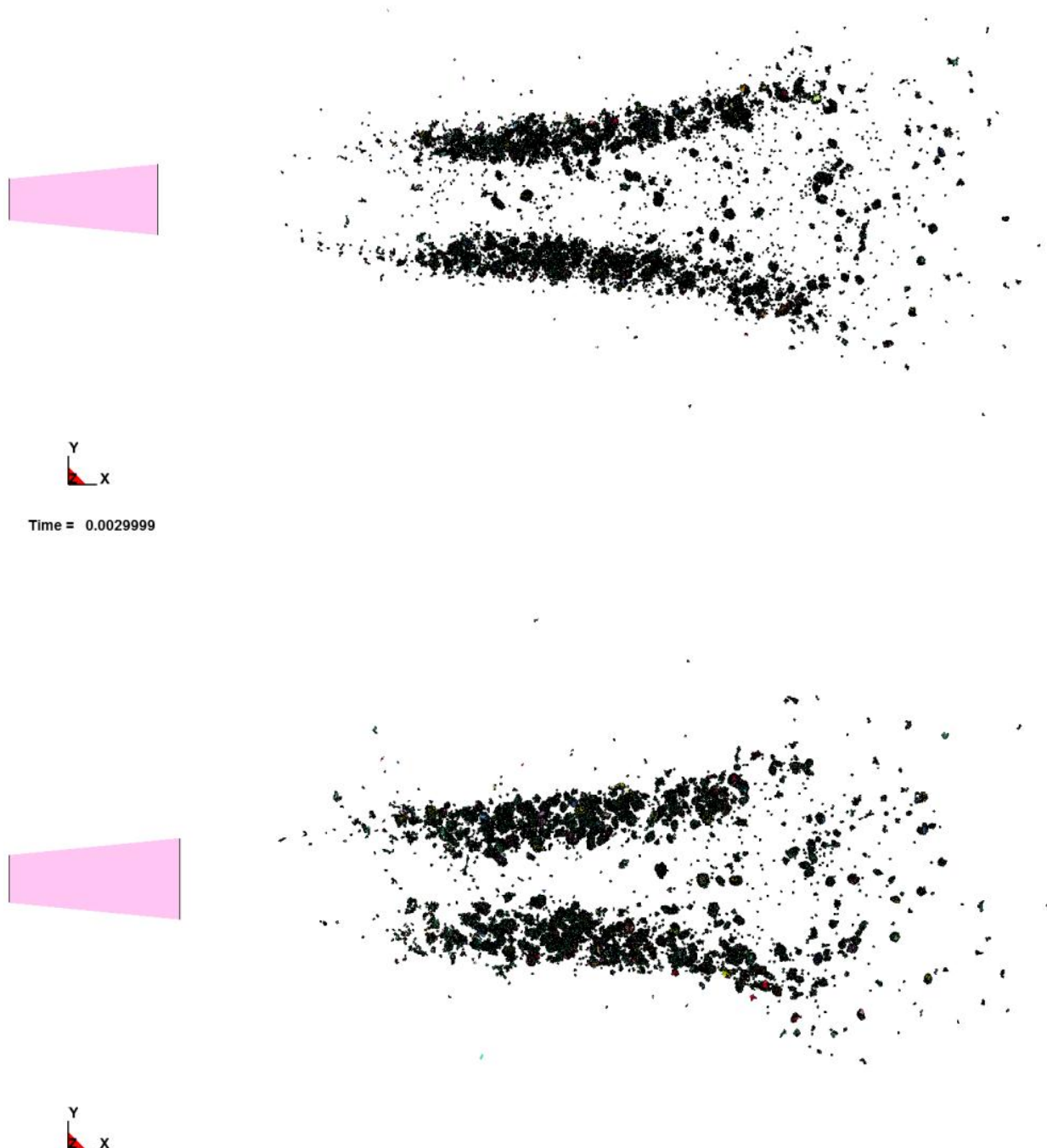


Figure 4.7: **Al7039 RVE at $t = 3 \mu\text{s}$** : above) non-uniform, strong border, porosity 10 %, below) non-uniform, strong border, porosity 20 %.

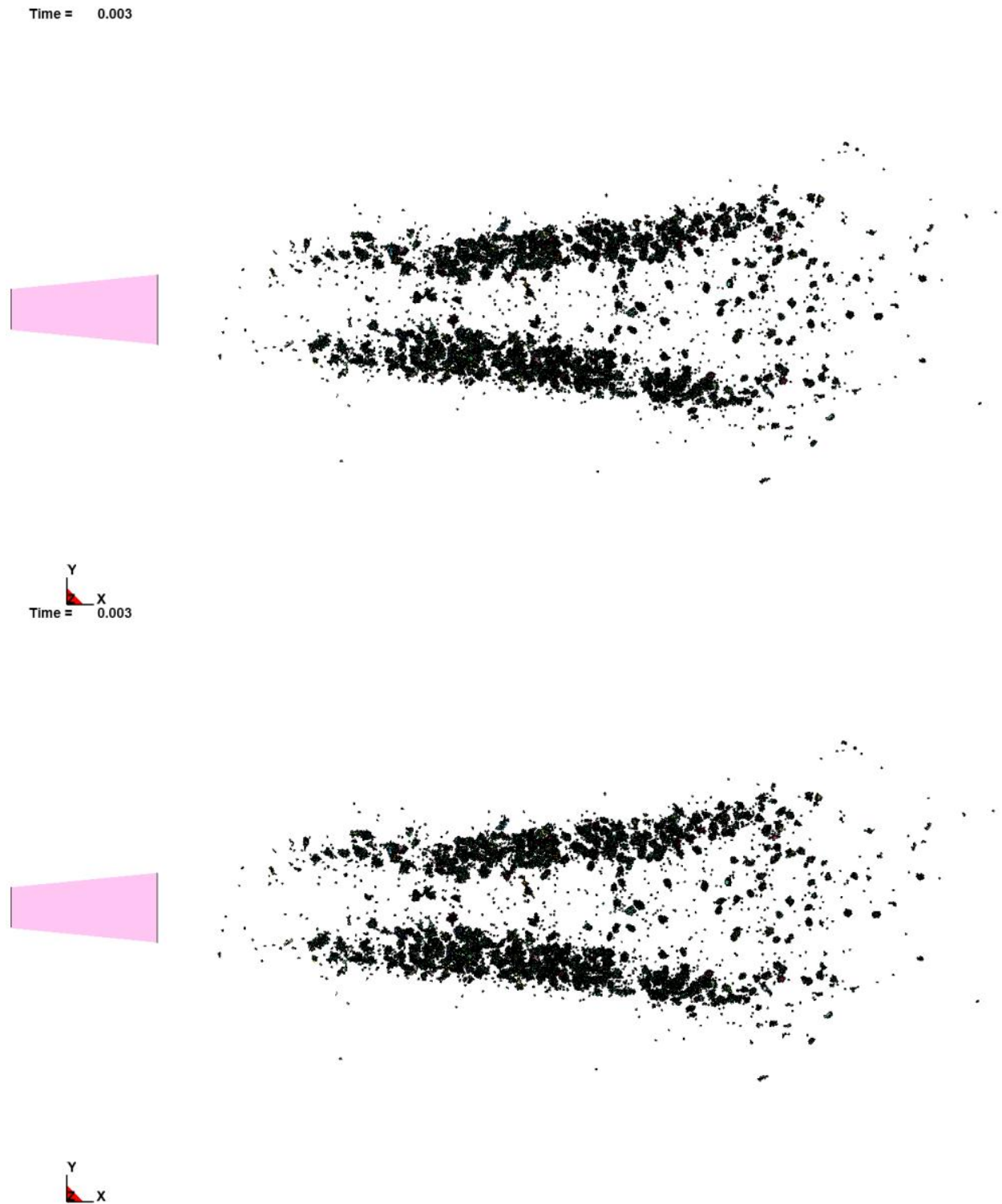


Figure 4.8: **Al7039 RVE at $t = 3 \mu s$** : above) uniform, strong border, porosity 10 %, below) uniform, strong border, porosity 20 %.

Time = 0.003



Y
Time = 0.003
X

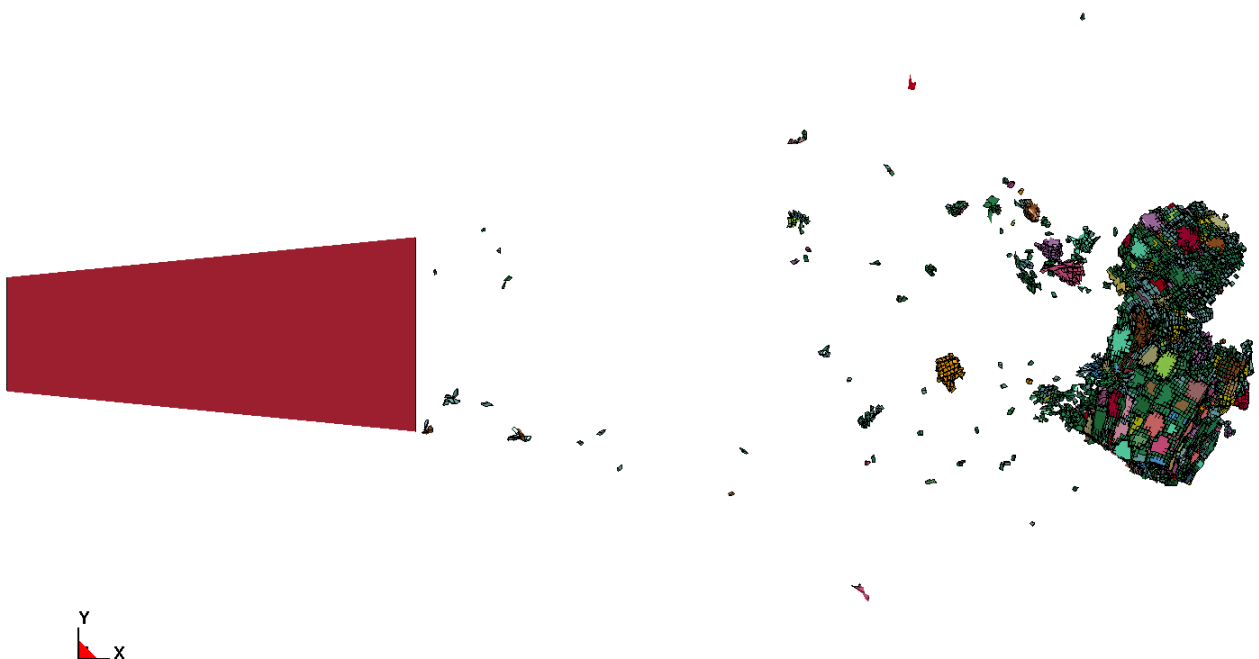


Figure 4.9: **Al₂₅/W₇₅ RVE at $t = 3 \mu\text{s}$** : above) non-uniform, strong border, porosity 10 %, below) non-uniform, strong border, porosity 20 %.

Time = 0.0029999



Time = 0.0029999

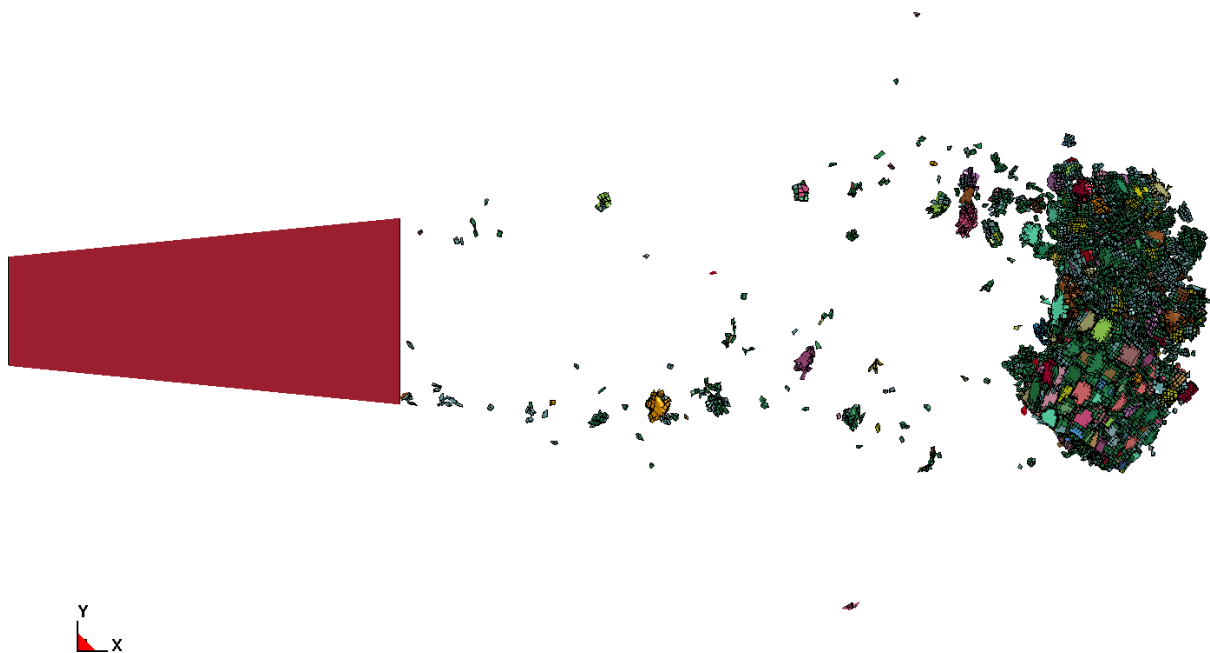


Figure 4.10: **Al₂₅/W₇₅ RVE at $t = 3 \mu\text{s}$** : above) non-uniform, weak border, porosity 10 %, below) non-uniform, weak border, porosity 20 %.

Time = 0.003



Y
X
Time = 0.003



Y
X

Figure 4.11: **Al₂₅/W₇₅ RVE at $t = 3 \mu\text{s}$** : above) uniform, strong border, porosity 10 %, below) uniform, strong border, porosity 20 %.

Time = 0.0029999



Time = 0.0029999

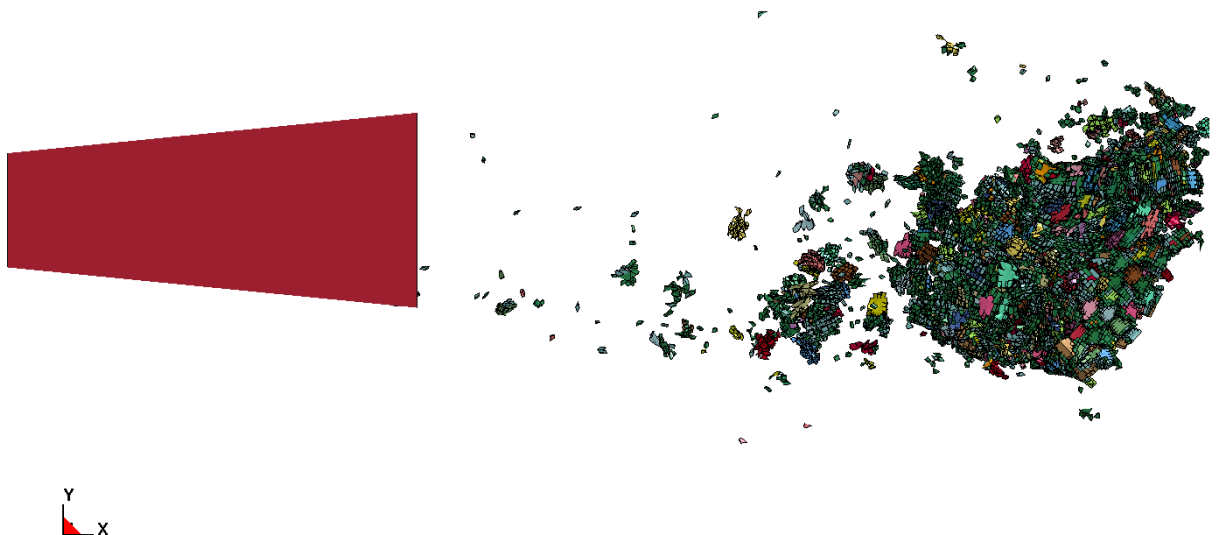
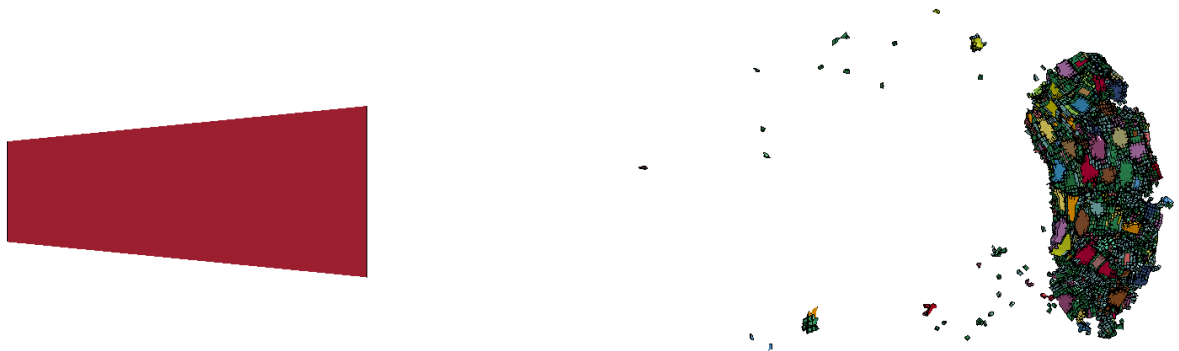


Figure 4.12: **Al₂₅/W₇₅ RVE at $t = 3 \mu\text{s}$** : above) uniform, weak border, porosity 10 %, below) uniform, weak border, porosity 20 %.

Time = 0.0029999



Y
Time = 0.003 X



Y
X

Figure 4.13: **Al38/W62 RVE at $t = 3 \mu s$** : above) non-uniform, strong border, porosity 10 %, below) non-uniform, strong border, porosity 20 %.

Time = 0.003



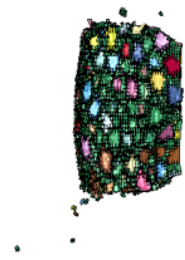
Y
X
Time = 0.0029999



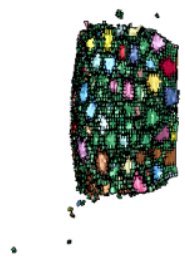
Y
X

Figure 4.14: **Al38/W62 RVE at $t = 3 \mu s$** : above) non-uniform, weak border, porosity 10 %, below) non-uniform, weak border, porosity 20 %.

Time = 0.0029999



Y
X
Time = 0.0029999



Y
X

Figure 4.15: **W RVE at $t = 3 \mu\text{s}$** : above) non-uniform, strong border, porosity 10 % below) non-uniform, strong border, porosity 20 %.

Time = 0.0029999



Y
X
Time = 0.0029999



Y
X

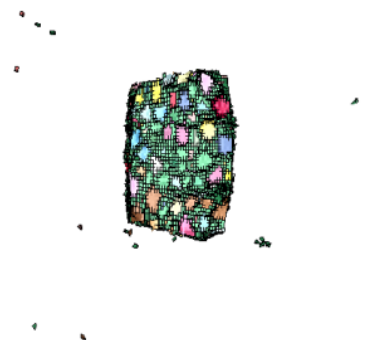
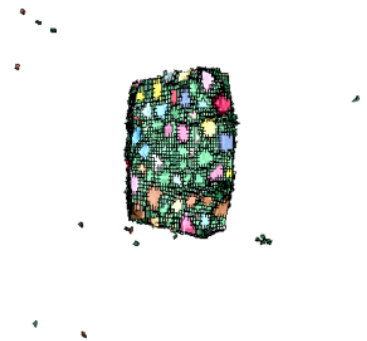


Figure 4.16: **W RVE at $t = 3 \mu\text{s}$** : above) non-uniform, weak border, porosity 10 %, below) non-uniform, weak border, porosity 20 %.

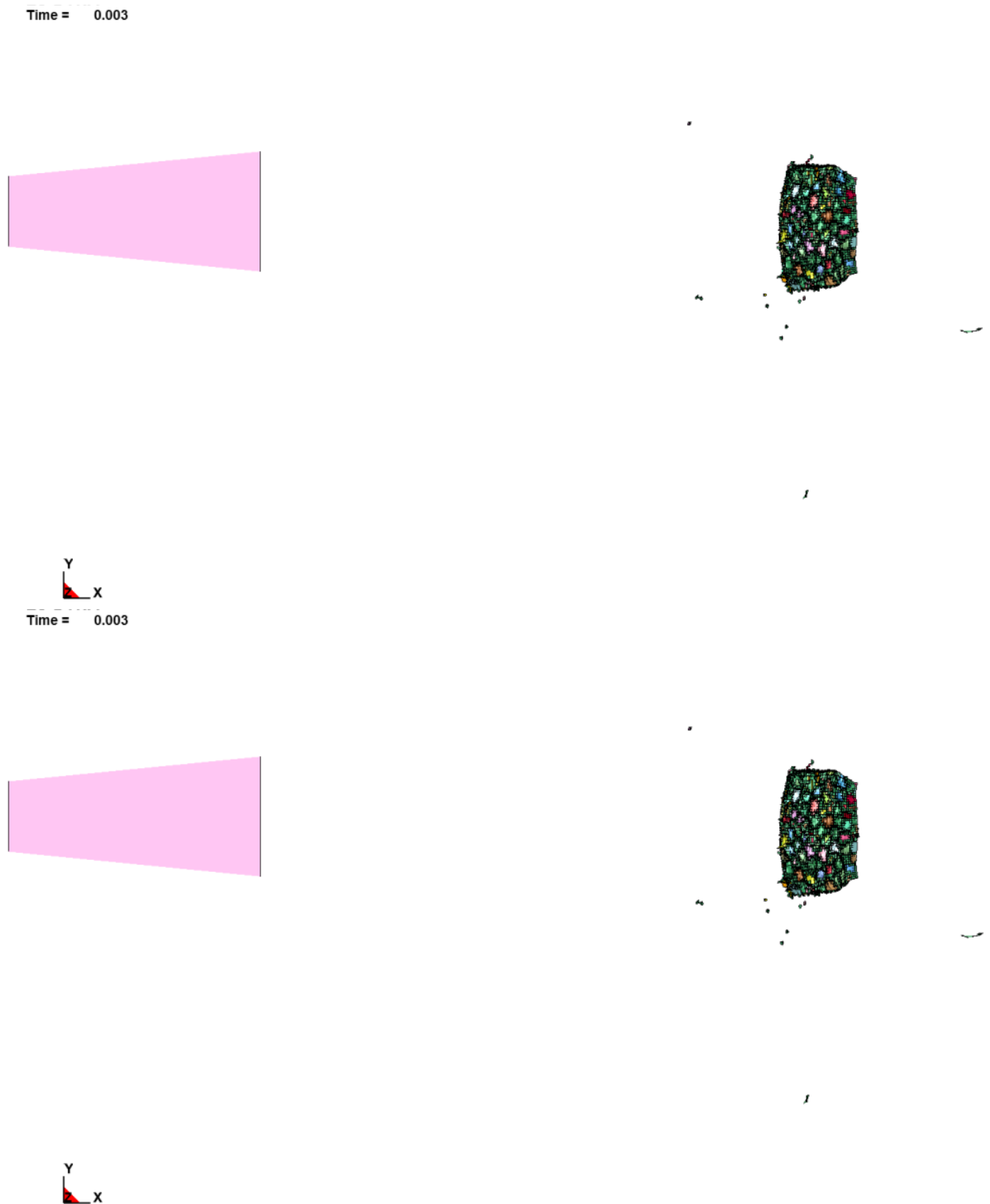


Figure 4.17: **W RVE at $t = 3 \mu\text{s}$** : above) uniform, strong border, porosity 10 %, below) uniform, strong border, porosity 20 %.

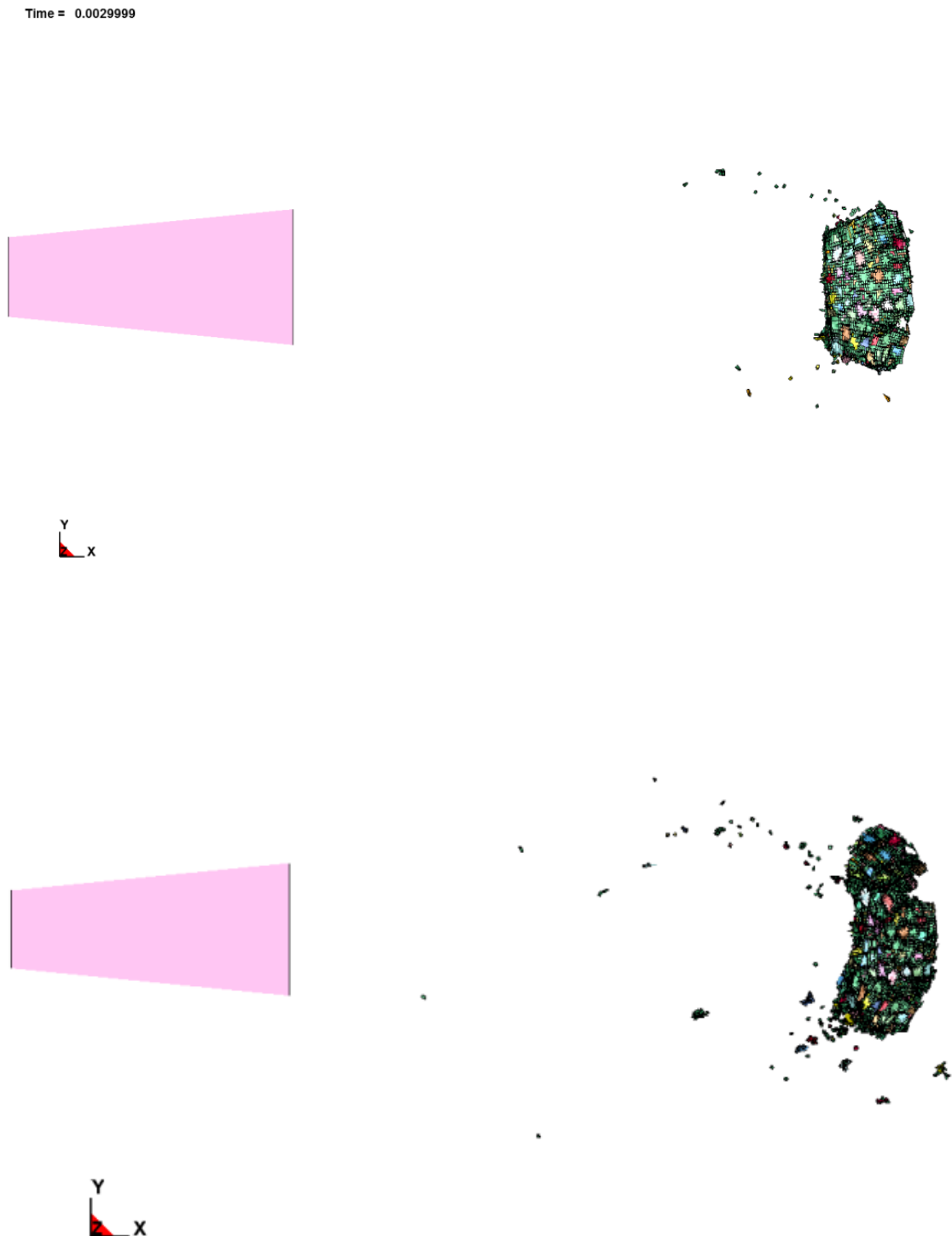


Figure 4.18: **W RVE at $t = 3 \mu\text{s}$** : above) uniform weak border, porosity 10 %, below) uniform, weak border, porosity 20 %.

Figure 4.19 shows the median fragment sizes for selected materials (with respect to cumulated fragment volume) that were obtained from the mesoscale simulations of the explosive launch.

In the diagram, it can be recognized that pure aluminum cubes do not survive the launch in the simulation. The median fragment sizes are nearly identical to the median grain size (about 37–39 μm for the uniform cases and about 42–45 μm for the non-uniform cases, c.f. Table 3.2) which indicates an almost total fragmentation.

The tungsten materials exhibit average fragment sizes of about 0.33 mm to 0.36 mm, which is close to the size of the scaled cube (edge length 0.3 mm; the diameter of the sphere with identical volume is approx. 0.37 mm). This indicates that only minor fragmentation occurs.

The W75/Al25 mixtures have fragment sizes which are only slightly lower than those of the pure tungsten which indicates that there is a certain chance that these materials survive the explosive launch intact. An exception is the variant “uniform/weak/porosity 20%”, which is the weakest mixture and shows considerable fragmentation.

Median Fragment Size after Launch

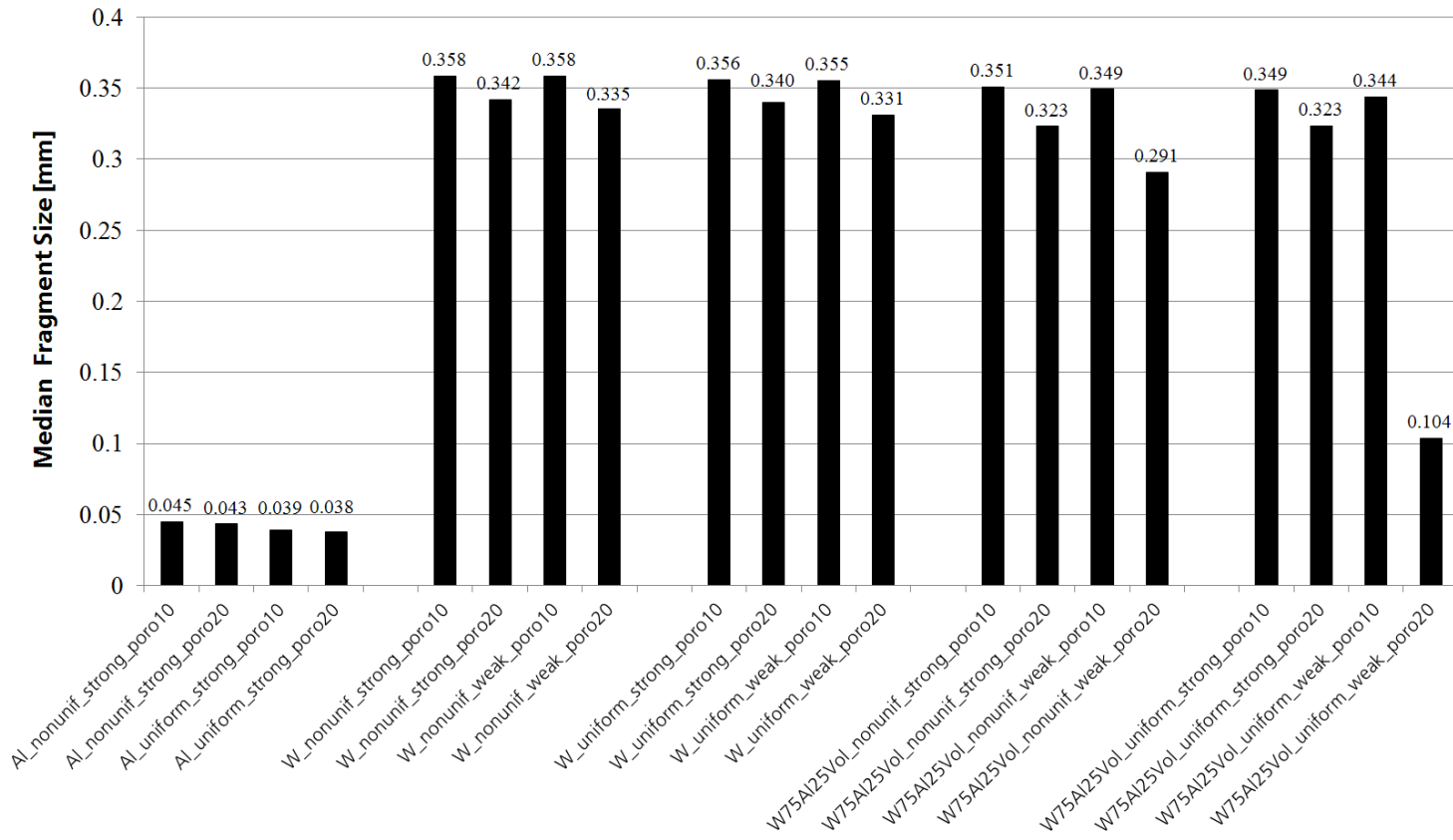


Figure 4. 19: Median fragment sizes (with respect to cumulated fragment volume) evaluated from launch simulations; fragment sizes given as diameter of volume-equivalent spheres.

5 Mesoscale Impact Simulations and Analysis

5.1 Impact Modeling

The computational model of the impact phase, see Figure 5.1, is an extension of the model used for the launch phase. The target plate has been positioned at a distance of 2.75 mm (90 mm in real scale) from the initial cube position, such that all cube variants were accelerated to their final velocities prior to the impact. As the impact simulations include the launch phase, the damage of the cube in the launch process is accounted for in the impact simulations.

The thickness of the target plate was 1 mm (scaled down to 0.03 mm). The target plate consisted of aluminum. It has been modeled with a Johnson-Cook strength model and a Mie-Gruneisen equation of state with the parameters listed in table 5.1. The complete Johnson-Cook model describes the yield stress as follows, [9]:

$$\sigma_Y = \left(\sigma_{Y0} + B \epsilon_{pl}^n \right) \left(1 + C \ln \left(\frac{\dot{\epsilon}}{\dot{\epsilon}_0} \right) \right) \left(1 - \frac{T - T_{room}}{T_{melt} - T_{room}} \right)$$

Table 5.1: Material properties of the aluminum target plate. The strength data refer to a standard grade aluminum (source: Fraunhofer EMI), EOS data is from Los Alamos report-4167-MS Selected Hugoniot (1969).

Density	$\rho = 2.76 \text{ g/cm}^3$
Shear modulus	$G = 25.8 \text{ GPa}$
Mie-Gruneisen EOS	$C_0 = 5328 \text{ m/s}$ $s1 = 1.338$ $\Gamma = 2$
Johnson-Cook flow stress	$\sigma_{Y0} = 0.2 \text{ GPa}$ $B = 0.36 \text{ GPa}$ $n = 0.34$ $C = 0.015$ $\dot{\epsilon}_0 = 1.0 \text{ 1/s}$ $T_{room} = 293 \text{ K}$ $T_{melt} = 775 \text{ K}$
Heat capacity	$C_p = 885 \text{ J/kg/K}$
Failure strain	$\epsilon_f = 1$

If the target plate is at rest, the cube impacts the plate with the final velocity achieved in the launch phase. Other impact velocities and angles of attack will be realized by imposing appropriate orientations and initial velocities of the target plate (Chapter 6). If the target plate is given an initial velocity the initial plate position is adjusted to ensure that the RVE reaches final velocity prior to impact.

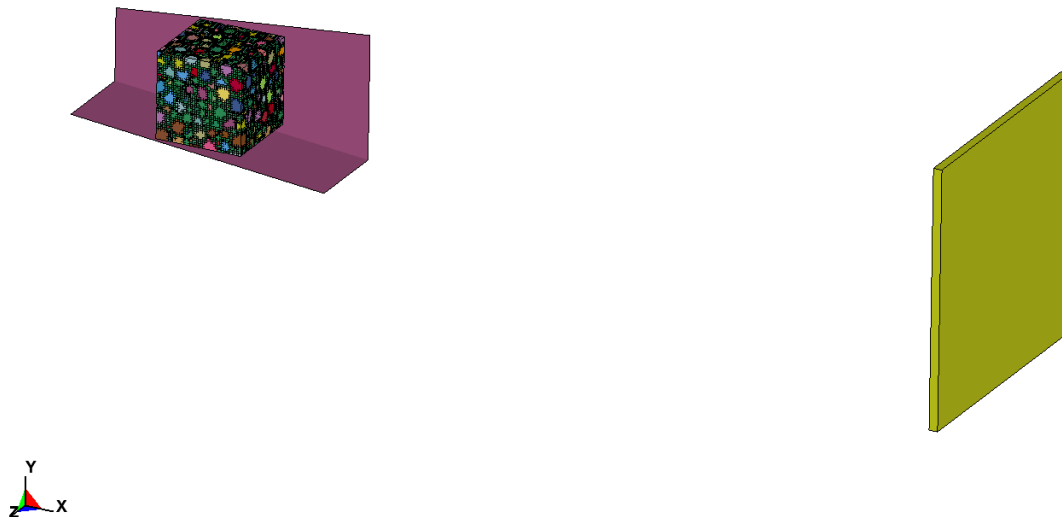


Figure 5.1: Numerical model for impact simulations (including launch phase).

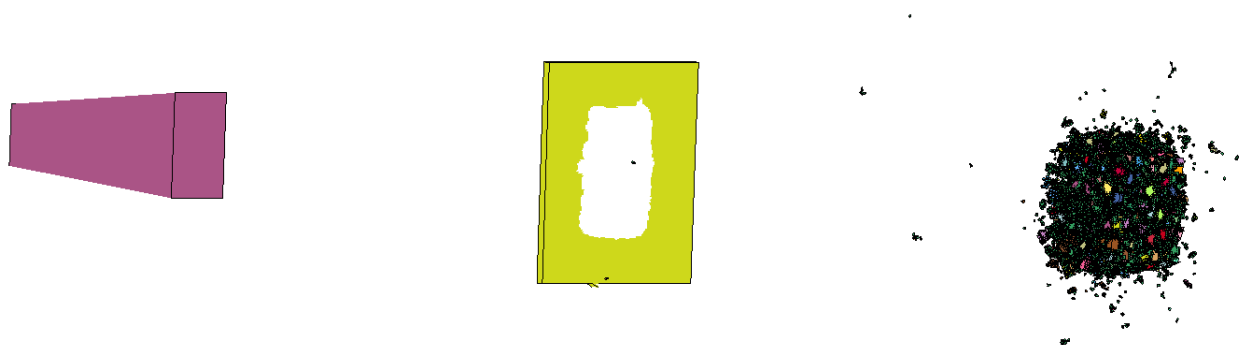


Figure 5.2: Results of an impact simulation. Rigid funnel, perforated impact plate and partially fragmented tungsten cube at scaled time 6 μ s.

5.2 Impact Simulation Results

The impact and fragmentation behavior of the material compositions which appear strong enough to survive the explosive launch have been investigated. These are the 100 % tungsten and the 25 % Al / 75 % tungsten mixtures with high intergranular strength, porosities of 10 % and 20 % and “uniform” and “non-uniform” structures, respectively.

The impact velocities for the pure tungsten cubes were in the range between 1050 m/s and 1150 m/s; for the mixture the impact velocities range from 890 m/s to 950 m/s. The variations occur due to small degrees of fragmentation during launch.

Figure 5.2 shows a representative simulation result. The picture is taken at scaled time of 6 μs (200 μs in original scale), i.e. about 3 μs after impact on the plate. One can see the hole in the perforated target plate and the partially fragmented cube on its right.

In Figures 5.3 to 5.6, the eight different investigated cubes are shown in enlarged visualizations at their state after impact (at 6 μs).

For both the tungsten cubes and the Al25/W75 cubes, the effects of the varied parameters are recognizable. As expected, the fragmentation increases with increasing porosity and decreasing inter-granular strength. The differences between "uniform" and "non-uniform" structures are less pronounced.

Tables 5.2 and 5.3 summarize the results for the investigated materials.

Figure 5.7 displays the primary results of the analysis of the impact and fragmentation process, which are the median fragment sizes after impact for the different materials. The maximum of the displayed values is 0.057 mm; some variants reach the value which corresponds to complete fragmentation (median value of about 0.037 mm to 0.039 mm for the "uniform" cases and about 0.042 mm–0.045 mm for the "non-uniform" cases).

As could be expected, the larger fragment sizes are observed for the stronger materials, i.e. the materials with low porosity and high inter-granular strength. No significant differences can be recognized between the cubes with "non-uniform" and "uniform" grain size distributions.

Based on these results, the composite with 75 % tungsten and 25 % aluminum with "non-uniform" grain size distribution, 10 % porosity and high inter-granular strength has been selected as most suitable material for the application as reactive material with perforation capability. The 100 % tungsten materials have less or no reactivity as they do not contain aluminum, they are therefore not considered.

In the next section, the impact scenario is varied in order to investigate the sensitivity of the fragmentation behavior on the impact conditions for the selected material.

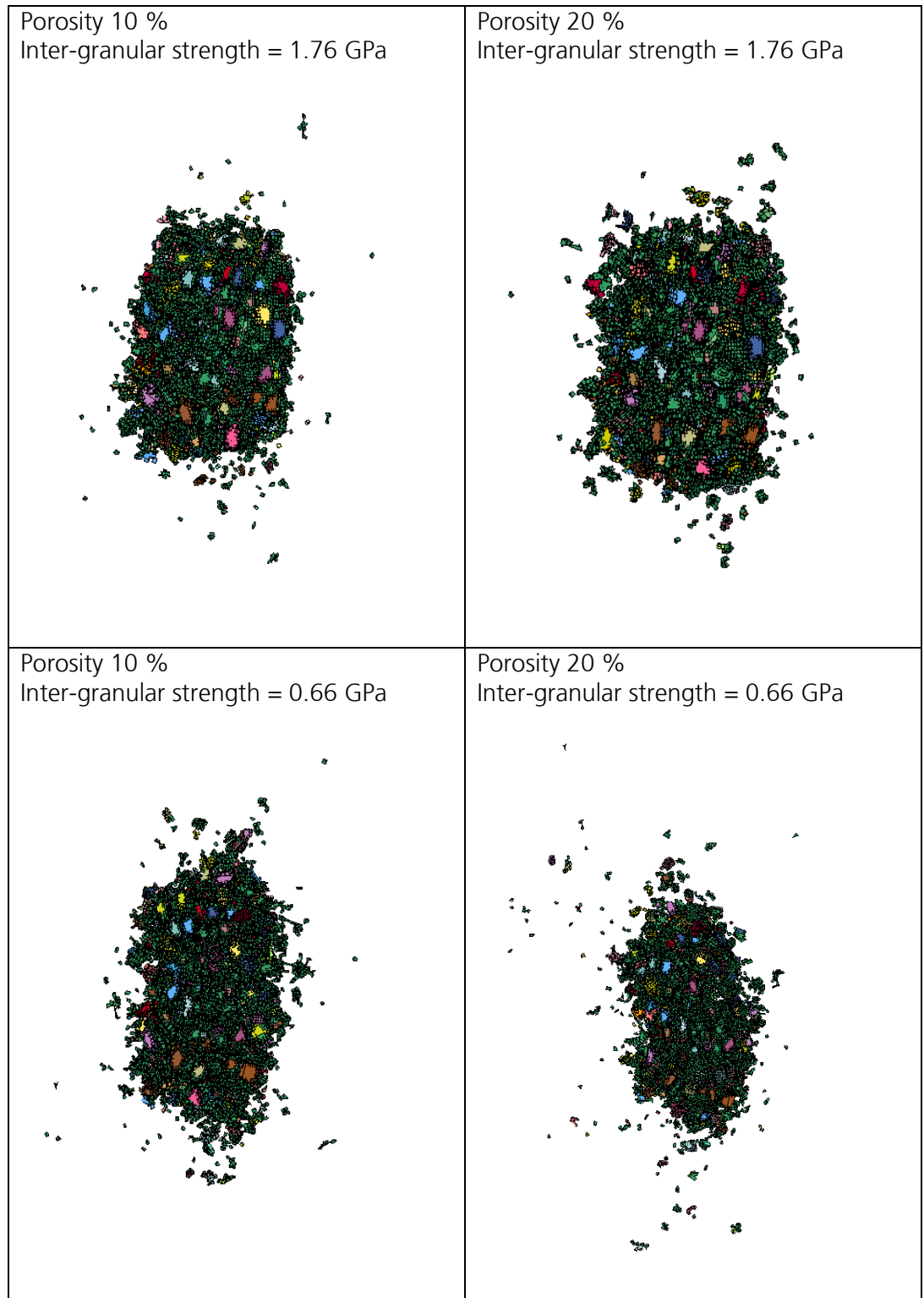


Figure 5.3: Partially fragmented “non-uniform” tungsten RVEs at scaled time 6 μ s.

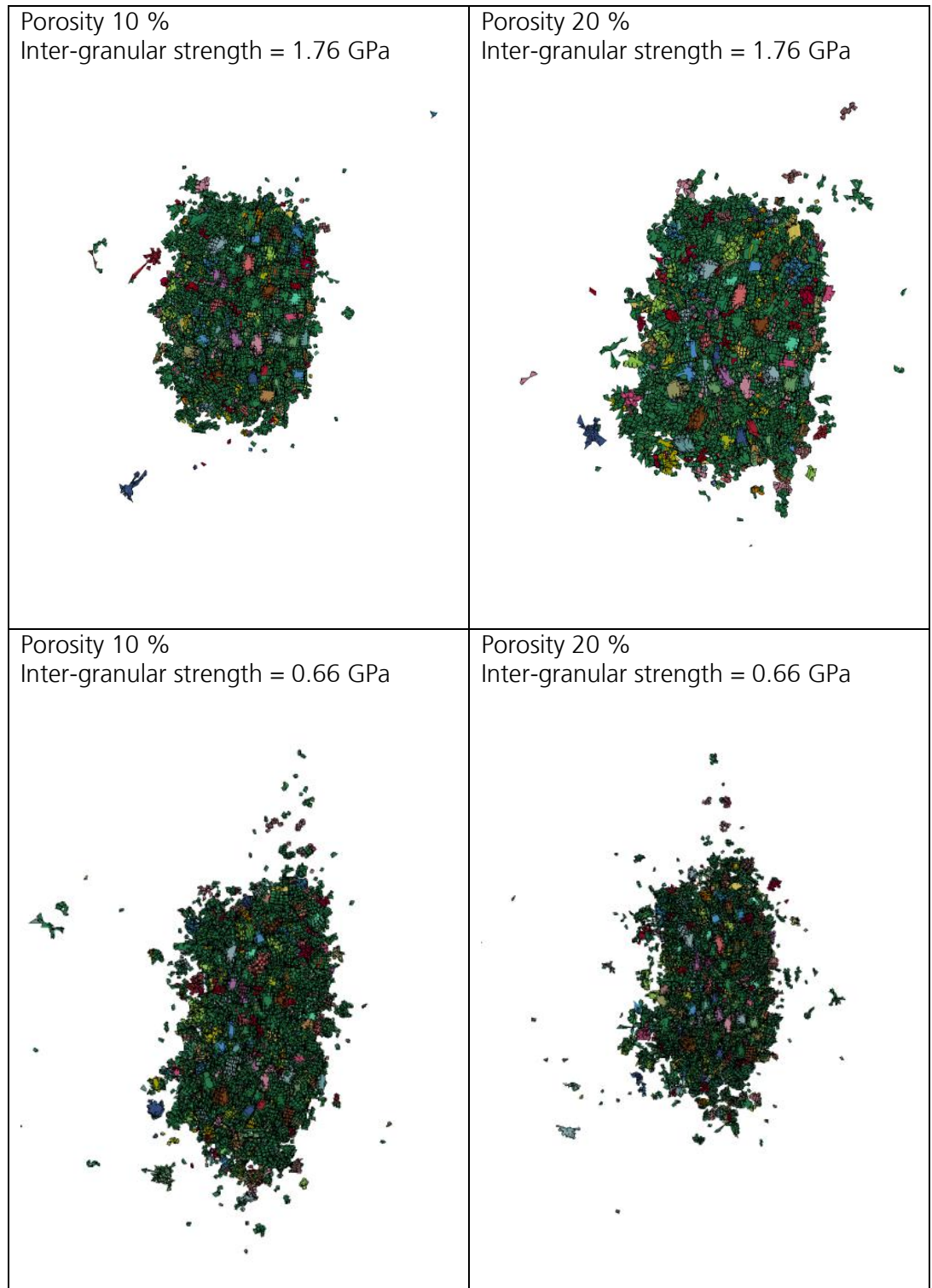


Figure 5.4: Partially fragmented “uniform” tungsten RVEs at scaled time 6 μ s.

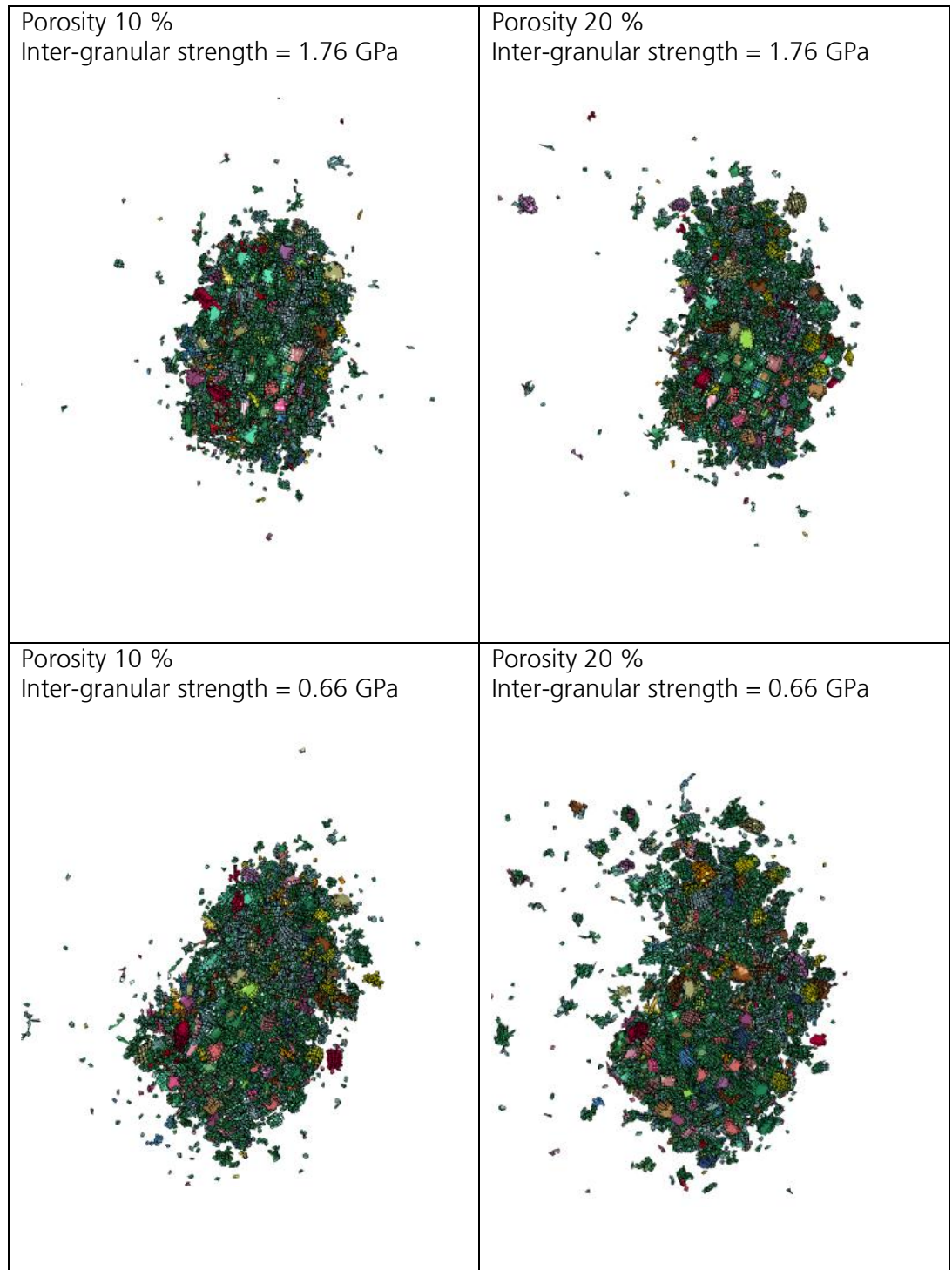


Figure 5.5: Partially fragmented “non-uniform” Al₂₅/W₇₅ RVEs at scaled time 6 μ s.

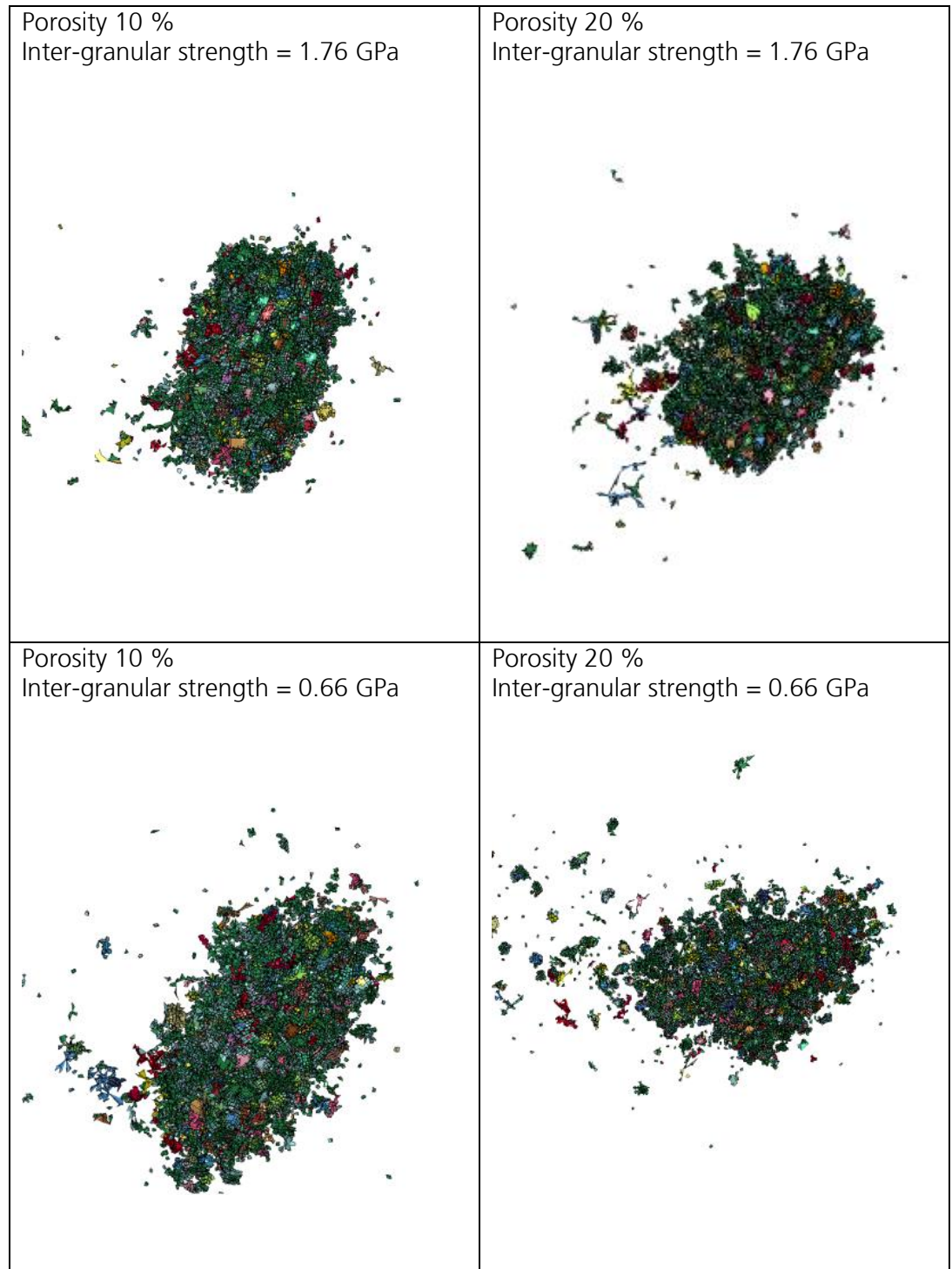


Figure 5.6: Partially fragmented “uniform” Al₂₅/W₇₅ RVEs at scaled time 6 μ s.

Table 5.2: Summary for the impact simulations with tungsten. The final (scaled) time is $t_{\max} = 6 \mu\text{s}$.

Mat.	Grain size distribution	Porosity [%]	Grain boundary strength [GPa]	Failure strain interval	Results		
					Damage state at t_{\max}	Velocity (t_{\max}) [m/s]	Displacement (t_{\max}) [mm]
W	Non-uniform	10	1.76	0.05 to 0.15	Damaged, many fragments, some larger fragments	1054.73	5.670
W	Non-uniform	20	1.76	0.05 to 0.15	Damaged, many fragments, few larger fragments	1052.42	5.807
W	Non-uniform	10	0.66	0.05 to 0.15	Damaged, many fragments, few larger fragments	1060.16	5.773
W	Non-uniform	20	0.66	0.05 to 0.15	Damaged, many fragments, very few larger fragments	1093.18	5.988
W	Uniform	10	1.76	0.05 to 0.15	Almost intact	1029.41	5.44
W	Uniform	20	1.76	0.05 to 0.15	Almost intact	1065.60	5.62
W	Uniform	10	0.66	0.05 to 0.15	Almost intact	1043.28	5.50
W	Uniform	20	0.66	0.05 to 0.15	Seriously damaged	1072.33	5.57

Table 5.3: Summary for the impact simulations with Al25/W75. The final (scaled) time is $t_{\max} = 6 \mu\text{s}$.

Mat.	Grain size distribution	Porosity [%]	Grain boundary strength [GPa]	Failure strain interval	Results		
					Damage state at t_{\max}	Velocity (t_{\max}) [m/s]	Displacement (t_{\max}) [mm]
Al25/W75	Non-uniform	10	0.32/1.76	0.05 to 0.15	Almost intact	878.72	4.73
Al25/W75	Non-uniform	20	0.32/1.76	0.05 to 0.15	Seriously damaged, many fragments,	880.40	4.80
Al25/W75	Non-uniform	10	0.32/0.66	0.05 to 0.15	Seriously damaged, many fragments, few larger fragments	914.06	4.86
Al25/W75	Non-uniform	20	0.32/0.66	0.05 to 0.15	Seriously damaged, many fragments, few larger fragments	934.29	4.92
Al25/W75	Uniform	10	0.32/1.76	0.05 to 0.15	Damaged	919.32	4.90
Al25/W75	Uniform	20	0.32/1.76	0.05 to 0.15	Seriously damaged	848.73	4.58
Al25/W75	Uniform	10	0.32/0.66	0.05 to 0.15	Seriously damaged	928.92	4.95
Al25/W75	Uniform	20	0.32/0.66	0.05 to 0.15	Totally damaged	872.06	4.64

Median Fragment Size after Impact

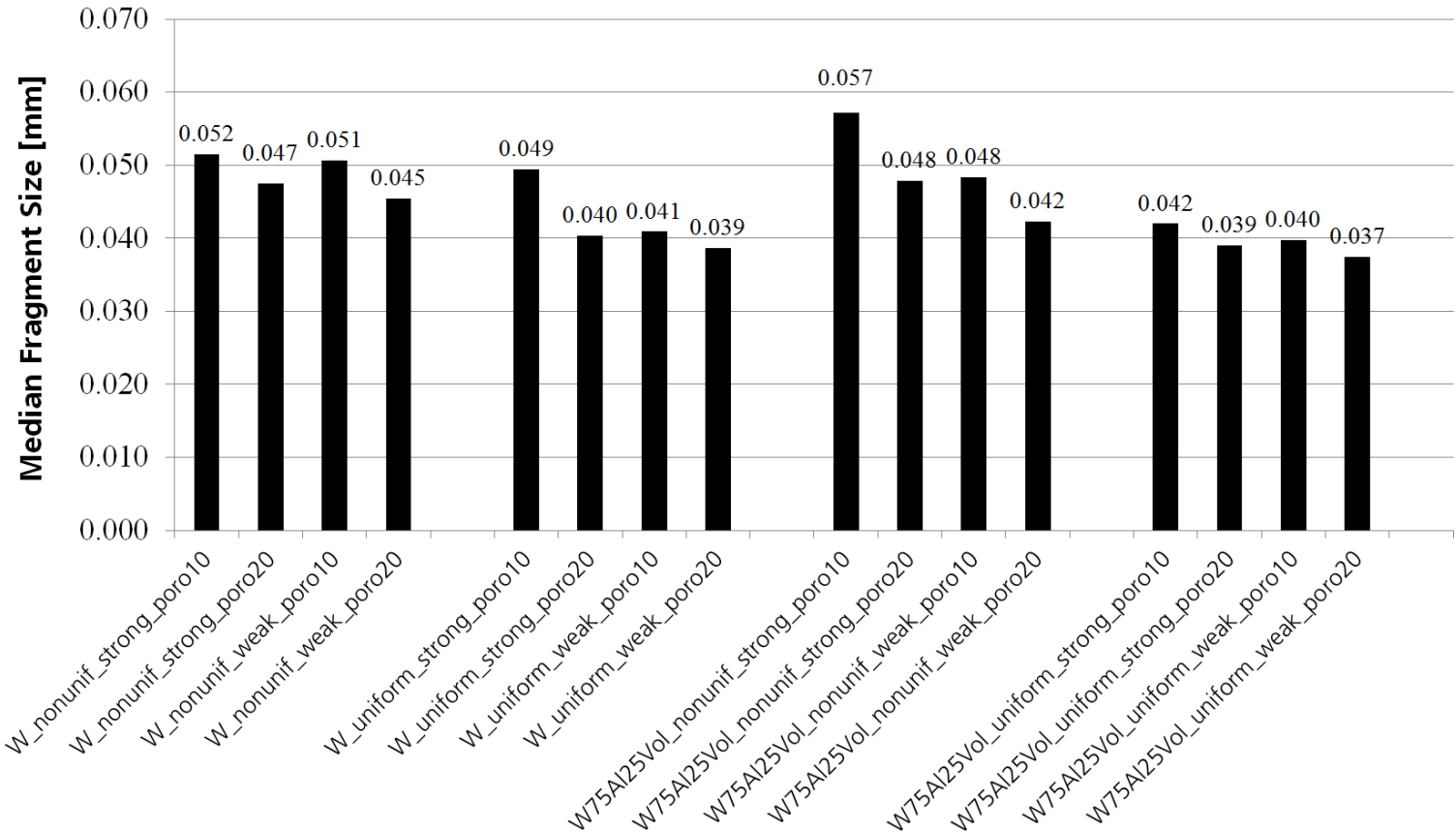


Figure 5.6: Median fragment size (with respect to cumulated fragment volume) after impact; compare with median grain sizes in Table 3.2.

6 Further Impact Conditions

The impact and fragmentation behavior of a selected material has been further investigated for a range of practically relevant impact conditions.

The selected material was Al25/W75 with “non-uniform” grain size distribution, high inter-granular strength (W: 1.76 GPa, Al: 0.32 GPa) and a porosity of 10 %. This material has sufficient strength to survive the launch process, but also fragments to a high degree upon impact under the conditions investigated in Chapter 5.

The parameter variations concerned the target conditions, i.e. the angle of incidence, the plate thickness, the plate material and the relative velocity of the plate. The following values were used:

- Angle of incidence: 0°, 15°, 30°, 45°
- Plate thickness (original scale): 1 mm, 0.5 mm, 2 mm, 4 mm
- Plate material: Al 7039; Steel 1006
- Impact Velocity (approx.): 950 m/s, 700 m/s, 1400 m/s, 2000 m/s

The first values stated in the above lists are the conditions which were investigated in the simulations presented in Chapter 5.

Table 6.1 summarizes the parameter variations and gives an overview of the results.

Figure 6.1 shows the impact of the Al25/W75 cube (scaled size 0.3 mm) on the aluminum target plate with an impact angle of 45° at two perspectives at the scaled time 6 μ s. The inclined target plate is perforated and the cube is seriously damaged. Many fragments are produced, but only few larger fragments. The residual velocity is about 937 m/s.

Figure 6.2 shows the result for the aluminum target plate with 4 mm thickness (scaled to 0.12 mm) at zero angle of attack. The plate is perforated and the cube is seriously damaged, the residual velocity is about 956 m/s.

In Figure 6.3, the result for the impact plate made of Steel 1006 is shown. The plate is perforated and breaks into chunks which stay in front of the cube. The cube is damaged and has a residual velocity of about 904 m/s.

Figure 6.4 shows the residual cubes after impact onto 1 mm aluminum plates with different relative velocities. It can be recognized that the fragmentation slightly increases with increasing impact velocity.

Figure 6.5 shows the median fragment size after impact. As a reference, the Al25/W75 case with zero angle of attack and 1 mm aluminum plate at rest is plotted in red (case presented in chapter 5). The median fragment size is 0.057 mm for that case.

The median fragment size becomes larger (0.074 mm) for impact angles of 15°, but decreases again to 0.052 mm when the impact angle is further increased to 45°.

Furthermore, the diagram shows that the median fragment size is reduced for thicker or heavier target plates, while the median value becomes significantly larger when the target plate thickness is reduced to one half of the reference value.

The median fragment size also decreases monotonically with increasing impact velocity from about 0.064 mm at 700 m/s impact velocity to about 0.045 mm at 2000 m/s impact velocity.

In summary, it can be stated that the fragmentation behavior of the material appears quite robust for the range of considered impact conditions. Exceptions can be identified for small impact angles, low velocities and very thin target plates, where less fragmentation (larger median size values) was found in the simulations.

Table 6.1: Summary for the impact simulations with Al25/W75 for different variations (see remark).
The final scaled time is $t_{\max} = 6 \mu\text{s}$.

Mat.	Grain size distribution	Porosity [%]	Grain boundary strength [GPa]	Remark	Results		
					Damage state at t_{\max}	Velocity (t_{\max}) [m/s]	Displacement (t_{\max}) [mm]
Al25/W75	Non-uniform	10	0.32,1.76	Al Plate angle 15 °	Seriously damaged, many fragments, some larger fragments	984.16	4.88
Al25/W75	Non-uniform	10	0.32,1.76	Al Plate angle 30 °	Seriously damaged, many fragments, few larger fragments	907.42	4.83
Al25/W75	Non-uniform	10	0.32,1.75	Al Plate angle 45 °	Seriously damaged, many fragments, few larger fragments	937.21	4.85
Al25/W75	Non-uniform	10	0.32,1.76	Steel plate 1006	Seriously damaged, many fragments, very few larger fragments	903.90	4.79
Al25/W75	Non-uniform	10	0.32,1.76	Al plate half thickness 0.015 mm	Almost intact	941.29	4.96

Table 6.1 (continued): Summary for the impact simulations with Al25/W75 for different variations (see Remark). The final scaled time is $t_{\max} = 6 \mu\text{s}$.

Al25/ W75	Non-uniform	10	1.76	Al plate double thickness 0.06 mm	Almost intact	915.91	4.85
Al25/ W75	Non-uniform	10	1.76	Al plate fourfold thickness 0.12 mm	Damaged	955.95	4.78
Al25/ W75	Non-uniform	10	1.76	Al Plate $V_{\text{rel}} =$ 700 m/s	Damaged	922.20	4.92
Al25/ W75	Non-uniform	10	1.76	Al Plate $V_{\text{rel}} =$ 1400 m/s	Damaged	918.67	4.88
Al25/ W75	Non-uniform	10	1.76	Al Plate $V_{\text{rel}} =$ 2000 m/s	Seriously damaged	916.72	4.86

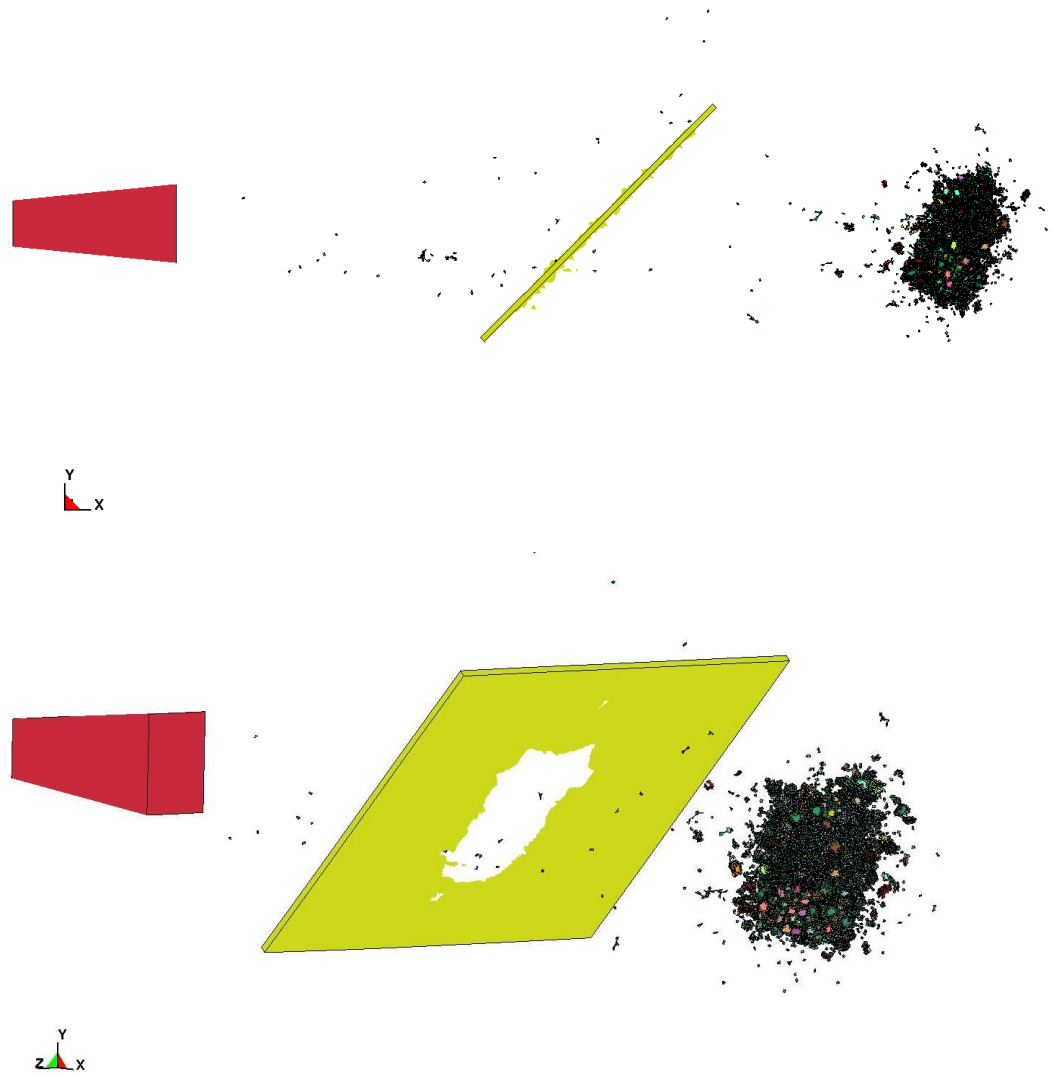


Figure 6.1: Impact of Al25/W75 RVE on Al-Plate with impact angle 45° at scaled time 6 μ s – two perspectives.



Figure 6.2: Impact of Al25/W75 RVE on Al-Plate with thickness 4 mm (scaled to 0.12 mm) at scaled time 6 μ s – two perspectives.

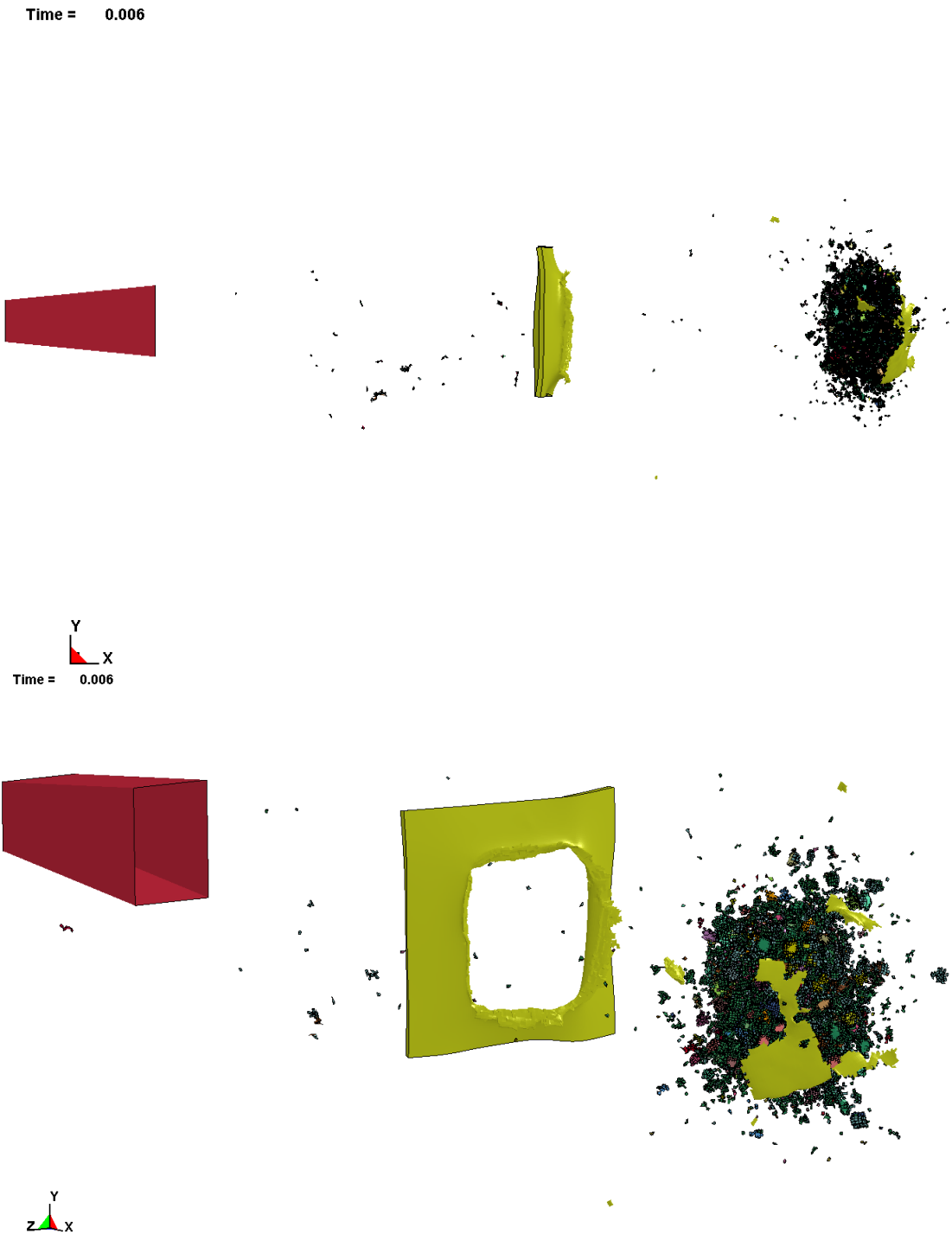


Figure 6.3: Impact of Al25/W75 RVE on steel 1006 plate with thickness 1 mm (scaled to 0.03 mm) at scaled time 6 μ s – two perspectives.

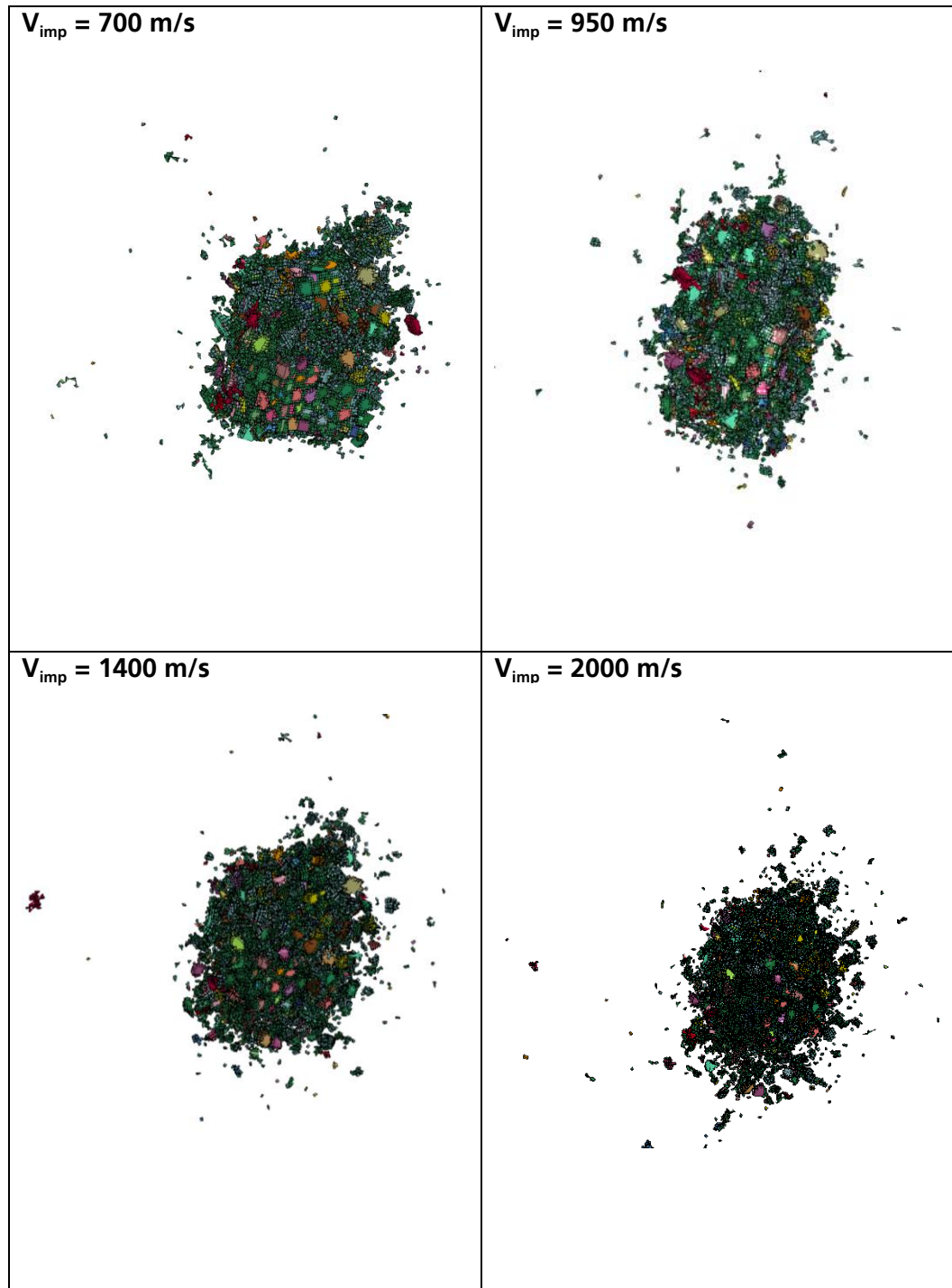


Figure 6.4: Fragmented Al25/W75 RVEs after impact on 1 mm Al target plate with different impact velocities.

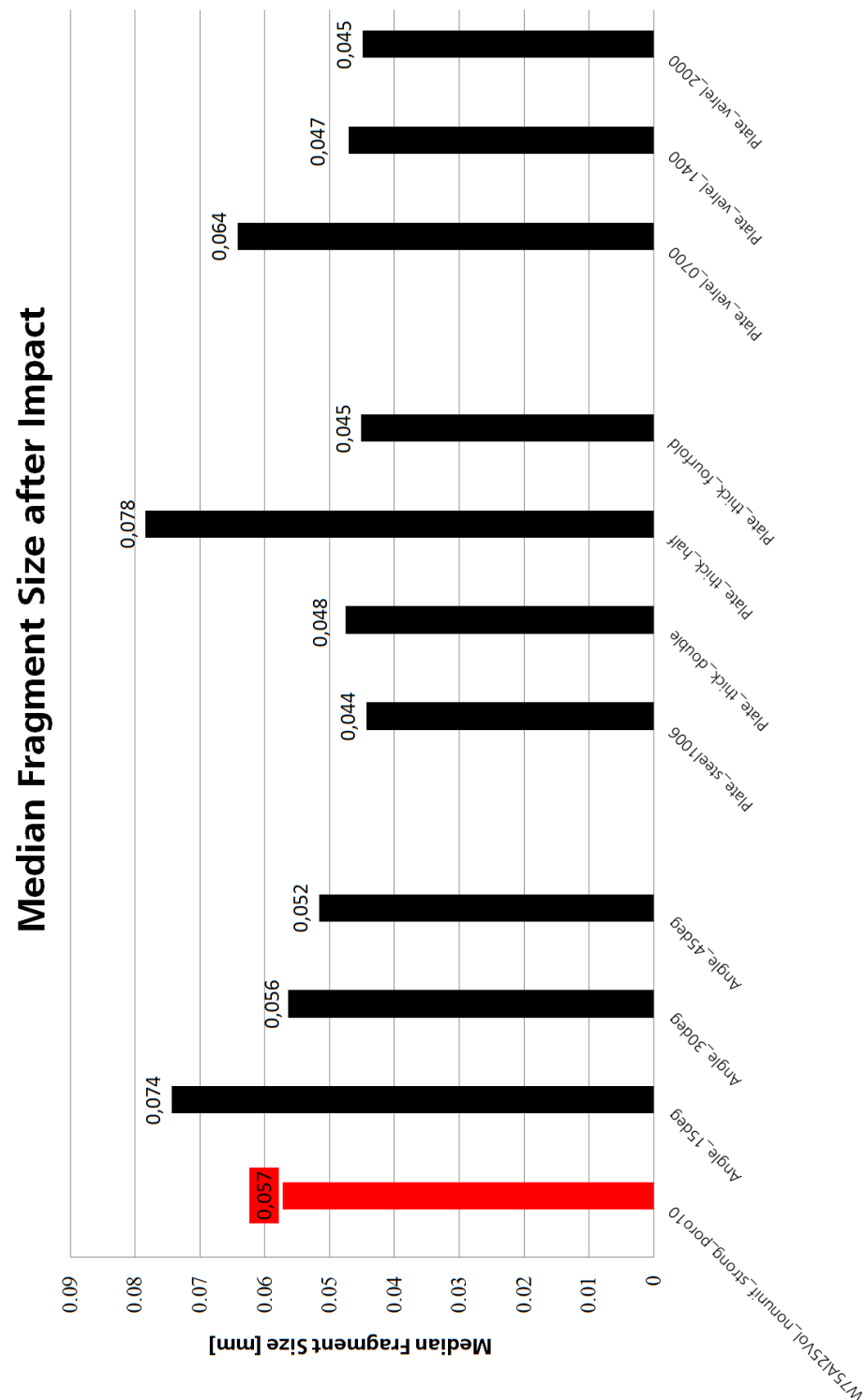


Figure 6.5: Median fragment size (with respect to cumulated fragment volume) after impact; compare with median grain sizes in Table 3.2.

7 Validity of the Scaling Concept

7.1 Assessment for Tensile Test Simulations

The effect of RVE size has been investigated for a few selected materials under quasi-static tensile loading. The selected materials were pure tungsten, pure aluminum and the Al25/W75 mixture, each with 10 % porosity, "non-uniform" grain size distributions and high inter-granular strengths.

The investigated RVEs had edge lengths of $L = 0.3$ mm, $L = 0.6$ mm and $L = 0.9$ mm, where the smaller RVEs are sub-volumes extracted from the largest RVE as shown in Figure 7.1. The differently sized RVEs thus have the same grain size statistics (c.f. Chapter 3).

The mesh resolution (finite element size) is the same for all three RVEs. It is $7.5\text{ }\mu\text{m}$, which corresponds to 120, 80 and 40 elements per edge for the three different RVE sizes, respectively. Compared to the average grain diameter (which ranges between $37\text{ }\mu\text{m}$ to $45\text{ }\mu\text{m}$ throughout all considered cases in this study), the smallest RVE measures about 10 average grains per edge, the largest correspondingly about 30 average grains per edge.

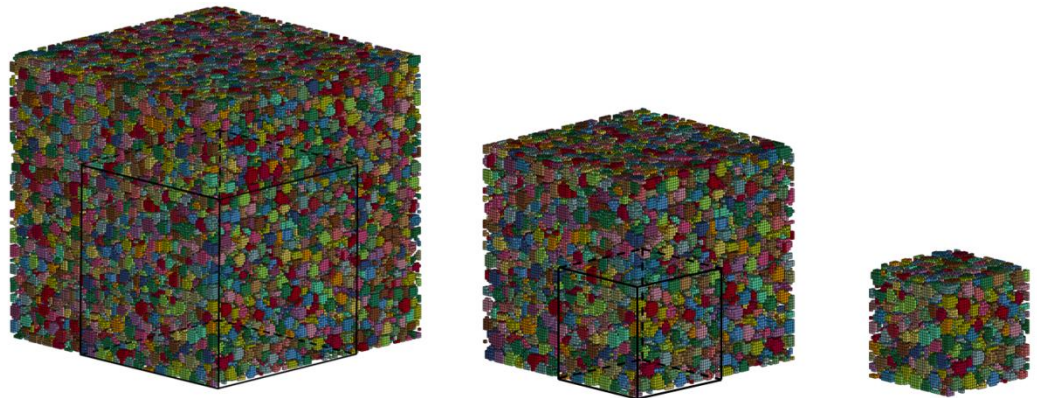


Figure 7.1: Three RVEs of different size. The middle and the smallest were extracted from the largest RVE. From left to right: $L = 0.9$ mm, $L = 0.6$ mm, $L = 0.3$ mm.

The uniaxial tensile tests were simulated for the different RVE sizes with strain rates in the order of about $1/s$; the actually applied velocity boundary conditions were adjusted such that an identical strain development over time was realized for the different materials.

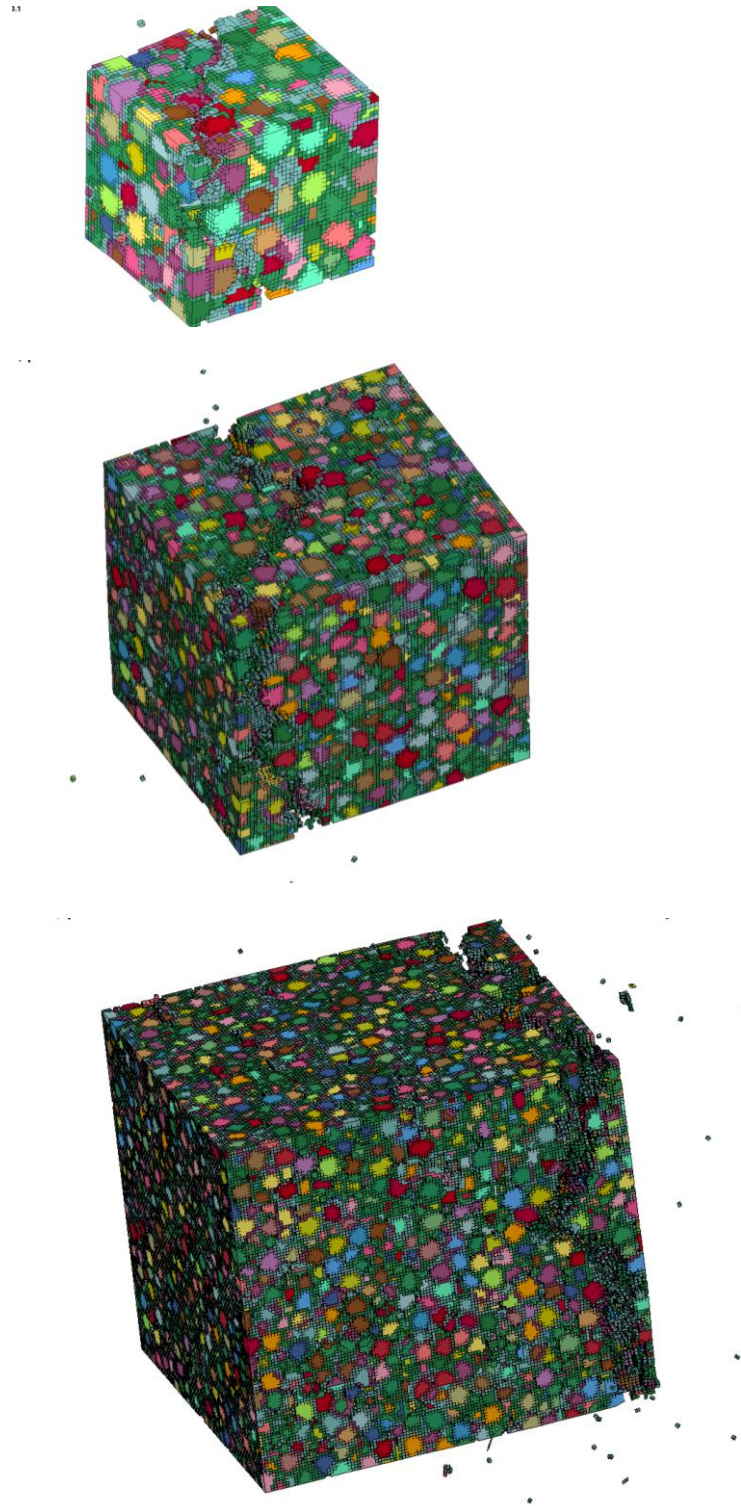


Figure 7.2: Al25/W75 RVE with size 0.3 mm, 0.6 mm and 0.9 mm (top to bottom) after fracture in tensile test simulations.

Figure 7.2 shows as an example the fractured states of the differently sized Al25/W75 RVEs. The pictures clearly show the essentially singular crack that goes through the RVEs.

A comparison of stress-strain curves is presented in Figure 7.3 for the different investigated materials. Note that the strain intervals of the damage region should be different – as they are – for the differently sized RVEs due to the different reference lengths used in the definition of strain. The remaining parts of the curves should however coincide for sufficiently large RVEs.

For the pure aluminum and the pure tungsten material, the 0.3 mm RVE size seems sufficient, as the stress-strain curves coincide well (remark: the simulation for the 0.9 mm RVE for tungsten was erroneous and could not be repeated due to time constraints; the CPU time was about 1 month.) For the mixed material, the 0.6 mm and the 0.9 mm RVEs yield approximately coinciding results. However, the 0.3 mm RVE seems insufficient.

Nevertheless, due to the long computing times for the 0.6 mm and 0.9 mm RVEs, the parameter studies presented in Chapters 4 to 6 had to be performed with the smallest RVE.

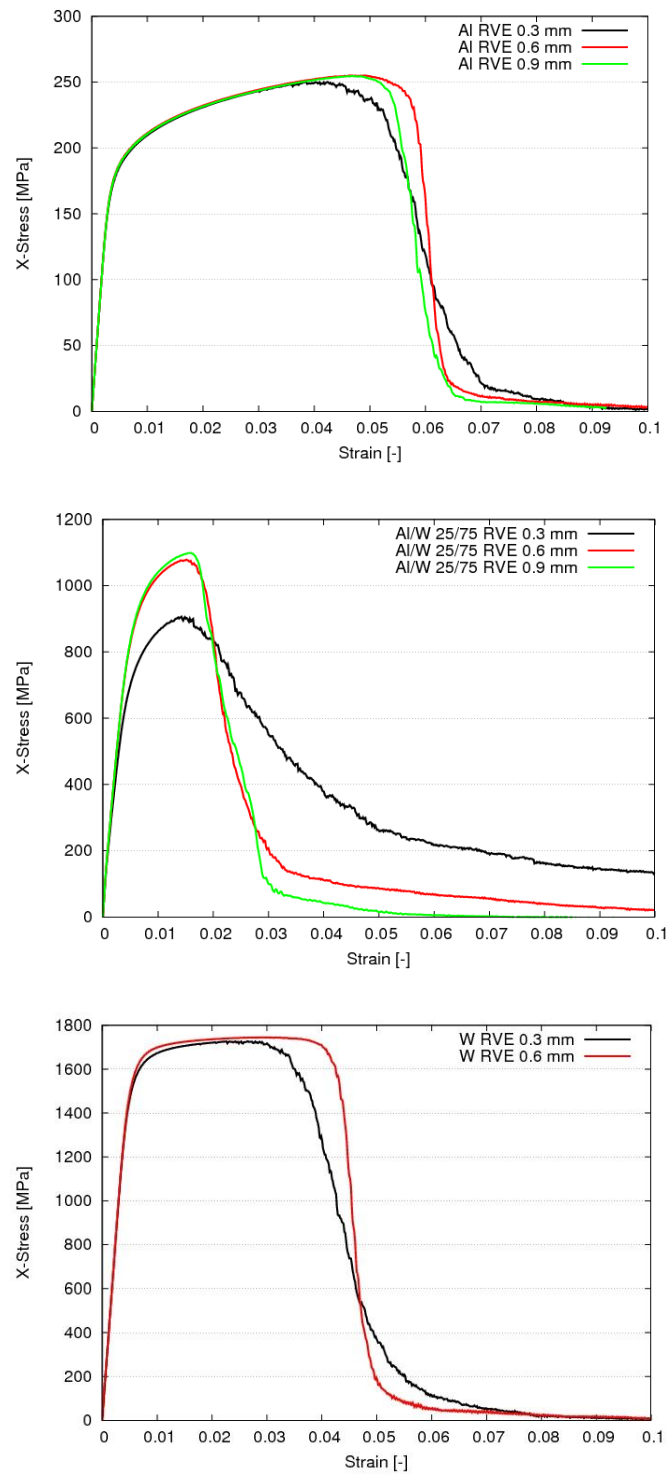


Figure 7.3: Stress-strain responses of statistically identical RVEs with different sizes for pure aluminum, Al25/W75 and pure tungsten materials (top to bottom).

7.2 Assessment for Impact Simulations

The effects of scaling on the macroscale were further investigated for both the launch and the impact process. The investigation with respect to the impact process was conducted at the beginning of the project. Therefore, already available material data from the previous project was used in this investigation.

The fragmentation of differently scaled cubes with identical grain size statistics were simulated for impacts on scaled aluminum target plates. The scaled cubes had edge lengths of 0.2 mm and 0.4 mm; the target plates had thicknesses 0.05 mm and 0.1 mm, respectively. Three different impact velocities of about 630 m/s, 1600 m/s and 2600 m/s were studied. An additional case with a 0.8 mm cube impacting a 0.2 mm plate was simulated for a velocity of 1600 m/s. The finite-element size was the same for all cases (8 μ m). The study was conducted for two different materials, CuFe 300 MPa and Fe 580 MPa (the pressure values refer to the fabrication pressure, c.f. [1]).

The different cases were compared with respect to the average fragment size, which was defined here as the median of the cumulative fragment volume distribution. The comparison is shown in Table 7.1.

Table 7.1: Average fragment volume (in 0.001 mm³) after impact of RVE against aluminum plate. Top: CuFe 300 MPa; bottom: Fe 580 MPa (material laws taken from [5]). Cases for which the average fragment volume is approximately unaffected by the scaling are marked green, other cases in yellow or red (strongly affected by scaling).

CuFe 300 MPa Unit: 0.001 mm ³	v = 634 m/s	v = 1600 m/s	v = 2600 m/s
L = 0.4 mm	0.169	0.109	0.093
L = 0.2 mm	0.257	0.106	0.094
Fe 580 MPa Unit: 0.001 mm ³	v = 475 m/s	v = 1600 m/s	v = 2600 m/s
L = 0.8 mm	–	283.2	–
L = 0.4 mm	54.5	30.1	0.118
L = 0.2 mm	7.18	3.69	0.117

For both materials, at the velocity of 2600 m/s, an identical average fragment volume for both cube dimensions was obtained. The same can be said for 1600 m/s for the CuFe mixture. For all other cases, significant deviations between both scales occur and no direct relation between fragment size and scale can be explicitly formulated.

From this, it can be concluded that there is an upper limit of the average fragment volume (or a lower limit of the impact velocity) beyond which the scaling significantly affects the fragmentation results.

The cubic root of the average fragment volume can be taken as a measure for the average fragment size. Using this measure, the ratio of the average fragment size to the cube length can be set up as a simple criterion for the a-posteriori assessment of the scaling.

In our case, the scaling seems to provide correct results for values of this ratio up to about 0.25, independently of impact velocity and material properties (c.f. Table 7.2). This suggests a universal applicability as a criterion to assess the scaling approach for cube impact on plates. The statement is that the scaling provides correct results if the cube edge length is at least four times larger than the obtained average fragment size.

The impact simulations presented in Chapters 5 and 6 satisfy this criterion.

Table 7.2: Ratio of average fragment size to cube length derived from values in Table 7.1. Top: CuFe 300 MPa; bottom: Fe 580 MPa. Cases for which the average fragment volume is approximately unaffected by the scaling are marked green, other cases yellow.

CuFe 300 MPa	v = 634 m/s	v = 1600 m/s	v = 2600 m/s
	$L_{\text{frag}}/L_{\text{cube}}$	$L_{\text{frag}}/L_{\text{cube}}$	$L_{\text{frag}}/L_{\text{cube}}$
$L_{\text{cube}} = 0.4 \text{ mm}$	0.14	0.12	0.11
$L_{\text{cube}} = 0.2 \text{ mm}$	0.32	0.23	0.22
Fe 580 MPa	v = 475 m/s	v = 1600 m/s	v = 2600 m/s
	$L_{\text{frag}}/L_{\text{cube}}$	$L_{\text{frag}}/L_{\text{cube}}$	$L_{\text{frag}}/L_{\text{cube}}$
$L_{\text{cube}} = 0.8 \text{ mm}$	-	0.825	-
$L_{\text{cube}} = 0.4 \text{ mm}$	0.95	0.78	0.12
$L_{\text{cube}} = 0.2 \text{ mm}$	0.95	0.75	0.24

7.3 Assessment for Launch Simulations

Launch simulations using differently scaled cubes with identical grain size statistics were conducted for two selected materials to check the validity of the scaling approach for the launch process. The scaled cubes had edge lengths of 0.3 mm and 0.6 mm. The simulations were carried out for the material variants pure aluminum and Al25/W75, each with 10 % porosity, high inter-granular strength and "non-uniform" grain size distribution.

The comparisons of the corresponding results are presented in Figures 7.3 and 7.4.

For the pure aluminum material, the accelerated cubes of both sizes were fully destructed during the acceleration; similar spatial distributions of the fragments can be recognized in Figure 7.3.

For the case with AL25/W75, the finding is that the smaller cube survives the simulated launch mainly intact, while the simulations with the larger scale predict a fracture of the cube in two parts and some erosion at the cube surfaces.

This means that the results of the launch simulations cannot be scaled up easily: Although a material variant, the AL25/W75 material, has been selected such that a 0.3 mm cube made of that material withstands the launch, the material does not fully withstand the launch if the cube is studied at larger scale.

This finding corresponds to the results obtained in the previous section: the scaling is only valid if the obtained fragments are considerably smaller than the size of the fragmenting object. In the scaled launch simulations, no fragmentation occurred, but this finding obviously cannot be transferred to larger scales.

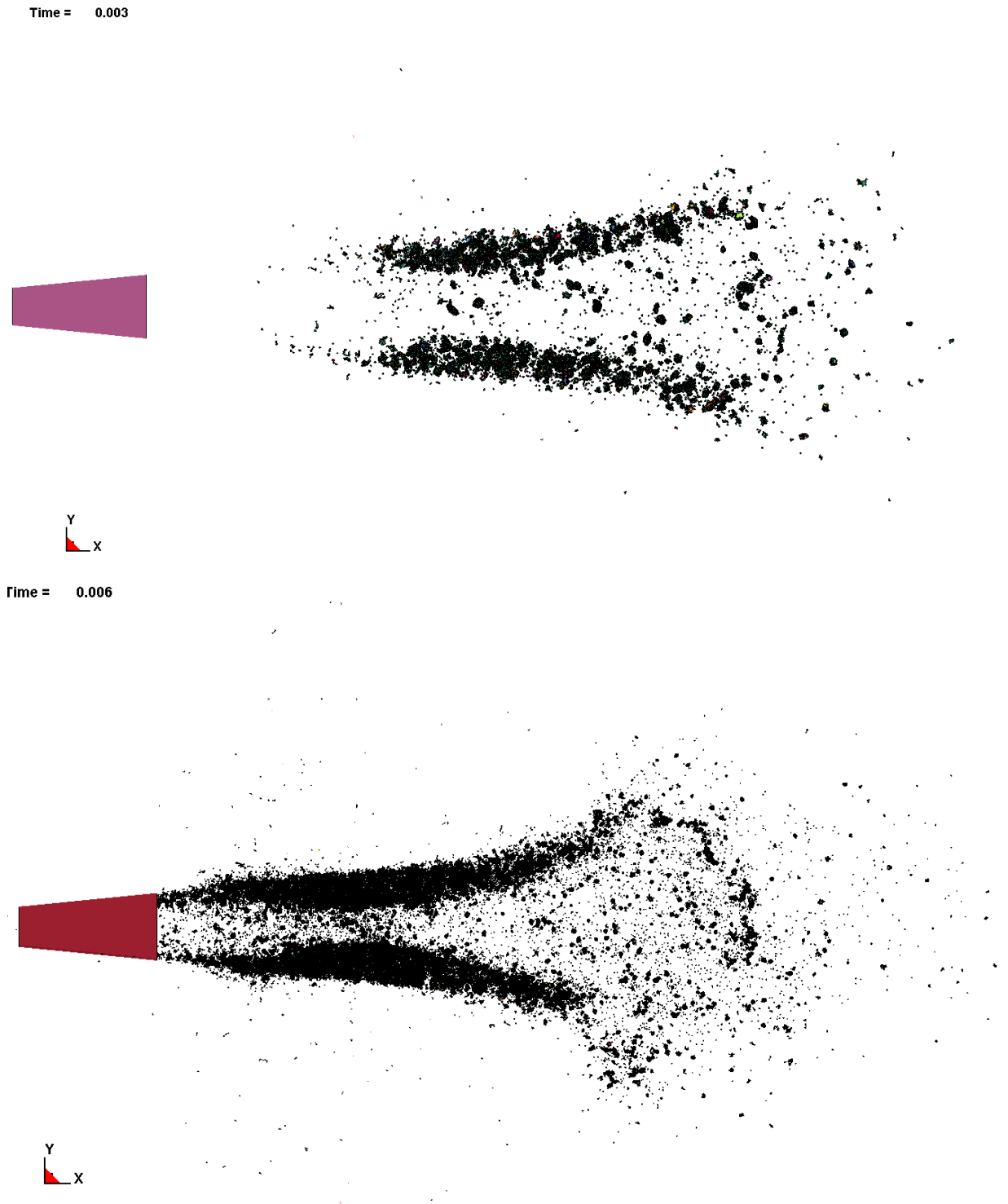


Figure 7.3: Results from launch simulations for pure aluminum cubes with cube sizes 0.3 mm (top) and 0.6 mm (bottom).

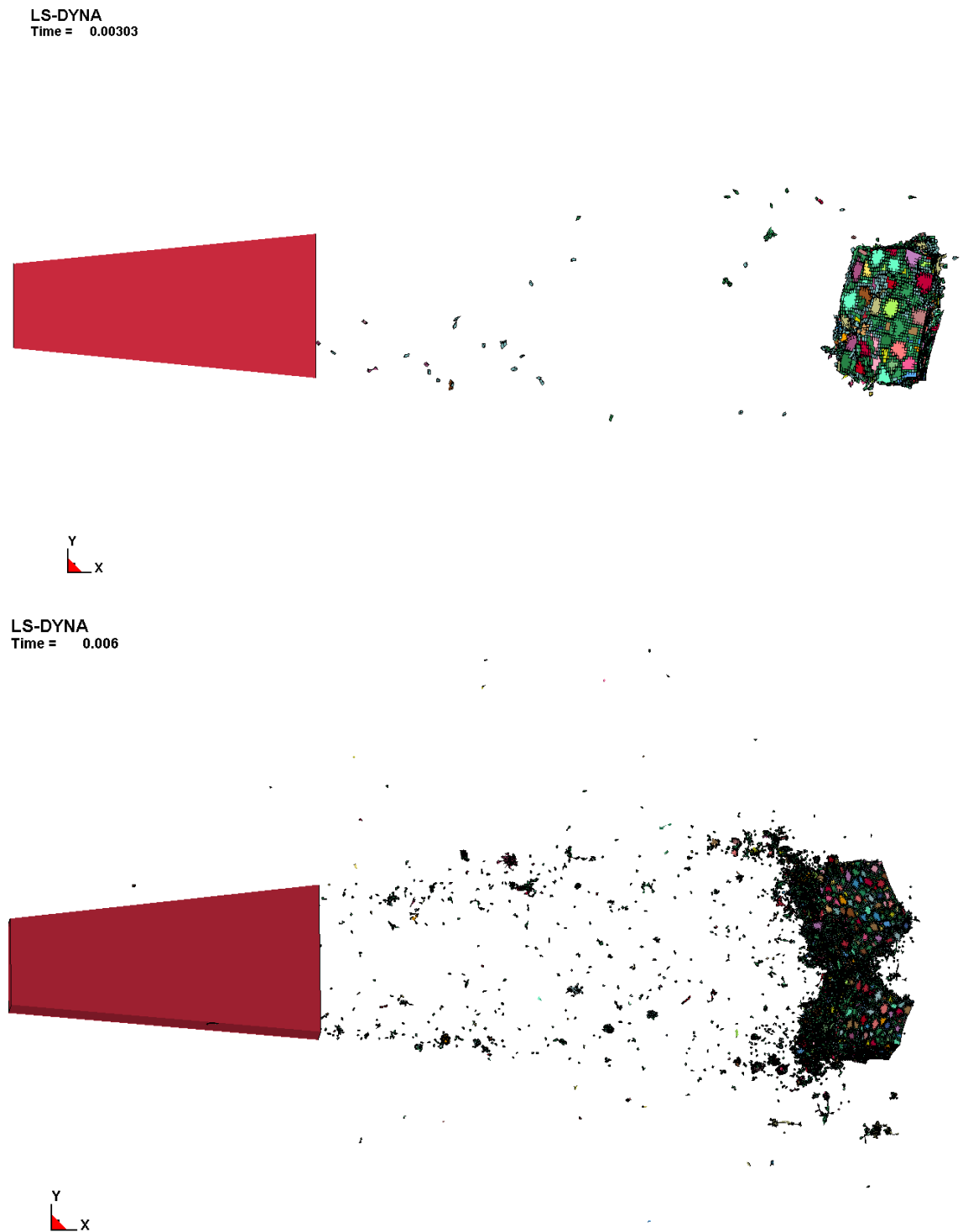


Figure 7.4: Results from launch simulations for Al25/W75 cubes with cube sizes 0.3 mm (top) and 0.6 mm (bottom).

8 Literature

- [1] Sauer, M.; Klomfass, A.; Bagusat, F.; Durr, N.; Knell, S.; Linnemann, K.: *"Characterization of the Material Microstructure for Reactive Material Design"*, (ONR grant N00014-07-1-1053 final report). Fraunhofer Institute for High-Speed Dynamics, Ernst-Mach-Institut, EMI, Freiburg, Germany, Report I-14/10, 2010
- [2] Sauer, M.; Bagusat, F.; Durr, N.; Klomfass, A.: *"Fragmentation of Partially Sintered Materials – Experimental Investigation and Mesoscale Simulation"*, Proceedings of the Hyper Velocity Impact Symposium HVIS 2010, Freiburg, Germany
- [3] Raftenberg, M. N.; Mock, W. Jr.; Kirby, G. C.: *"Modeling the Impact Deformation of Rods of a Pressed PTFE/Al Composite Mixture"*, Int. J. Imp. Eng. 35(12), 2008, pp. 1537–1544
- [4] Klomfass, A.; Bagusat, F.; Durr, N.; Heilig, G.; Knell, S.; Sauer, M.: *"Mesoscale Mechanics of Reactive Materials for Enhanced Target Effects"*, Report prepared for the 2011 Peer review of the Office of Naval Research 351 Advanced Energetics Materials and Advanced Combustion Program, National Harbor, MD, September 13–14, 2011
- [5] Heilig, G.; Durr, N.; Sauer, M.; Klomfass, A.: *"Mesoscale Mechanics of Reactive Materials for Enhanced Target Effects"*, Performance/Technical Report 2011, Report EMI I-56/11
- [6] Heilig, G.; Durr, N.; Sauer, M.; Klomfass, A.: *"Mesoscale Analysis of Sintered Metals Fragmentation under Explosive and Subsequent Impact Loading"*, Proceedings of the 12th Hypervelocity Impact Symposium, Baltimore, Maryland, September 16–20, 2012
- [7] Nossek, M.; Sauer, M.; Thoma, K.: *"Adaptive Simulation of Cohesive Interface Debonding for Crash- and Impact Analyses"*, Proceedings of the 3rd European Conference on Computational Mechanics: Solids, Structures and Coupled Problems in Engineering, Lissabon, 2006
- [8] Steinberg, D. J.: *"Equation of State and Strength Properties of Selected Materials"*, Lawrence Livermore National Laboratory, February 13, 1991
- [9] Johnson, G. R.; Cook, W. H.: *"A Constitutive Model and Data for Metals Subjected to Large Strains, High Strain Rates and High Temperatures"*, Proc. 7th Int. Symposium on Ballistics, The Hague, Netherlands, 1983

List of Distribution

Report No. I-69/12

Author: G. Heilig, N. Durr, M. Sauer, A. Klomfass

Title: Mesoscale Mechanics of Reactive Materials for Enhanced Target Effects
– Final Report 2012

Internal Distribution:

Author(s): G. Heilig, N. Durr, M. Sauer, A. Klomfass

External Distribution:

Clifford Bedford, Ph.D. 1 Hardcopy + CD
Program Manager Code 351
Advanced Energetics Materials
Office of Naval Research
875 N. Randolph St.
Arlington, VA 22203-1995

Dr. Judah Goldwasser
DARPA/DSO PDF
3701 North Fairfax Dr
Arlington, VA 22203
Judah.Goldwasser@darpa.mil

Defense Technical Information Center 1 Hardcopy + CD
8725 John J Kingman Road Ste 0944
Fort Belvoir, VA 22060-6218

ONR REG BOSTON N62879 1 Hardcopy + CD
495 Summer Street Room 627
Boston, MA 02210-2109

Naval Research Laboratory 1 Hardcopy + CD
ATTN: CODE 5596
4555 Overlook Avenue SW
Washington, DC 20375-5320

REPORT DOCUMENTATION PAGE				<i>Form Approved</i> <i>OMB No. 0704-0188</i>		
<small>The public reporting burden for this collection of information is estimated to average 1 hour per response, including the time for reviewing instructions, searching existing data sources, gathering and maintaining the data needed, and completing and reviewing the collection of information. Send comments regarding this burden estimate or any other aspect of this collection of information, including suggestions for reducing the burden, to Department of Defense, Washington Headquarters Services, Directorate for Information Operations and Reports (0704-0188), 1215 Jefferson Davis Highway, Suite 1204, Arlington, VA 22202-4302. Respondents should be aware that notwithstanding any other provision of law, no person shall be subject to any penalty for failing to comply with a collection of information if it does not display a currently valid OMB control number.</small> PLEASE DO NOT RETURN YOUR FORM TO THE ABOVE ADDRESS.						
1. REPORT DATE (DD-MM-YYYY) 17-12-2013		2. REPORT TYPE Final technical report		3. DATES COVERED (From - To) March 2012 - December 2012		
4. TITLE AND SUBTITLE Mesoscale Mechanics of Reactive Materials for Enhanced Target Effects - Final Report				5a. CONTRACT NUMBER		
				5b. GRANT NUMBER N00014-11-1-0307		
				5c. PROGRAM ELEMENT NUMBER		
6. AUTHOR(S) Klomfass, Arno, Dr. Sauer, Martin, Dr. Heilig, Georg, Dr. Durr, Nathanael				5d. PROJECT NUMBER		
				5e. TASK NUMBER		
				5f. WORK UNIT NUMBER		
7. PERFORMING ORGANIZATION NAME(S) AND ADDRESS(ES) FRAUNHOFER-INSTITUTE FOR HIGH SPEED DYNAMICS ECKERSTRASSE 4 FREIBURG 79104, GERMANY				8. PERFORMING ORGANIZATION REPORT NUMBER I-69/12		
9. SPONSORING/MONITORING AGENCY NAME(S) AND ADDRESS(ES) Clifford D. Bedford Office of Naval Research 875 North Randolph Street Arlington, VA 22203-1995				10. SPONSOR/MONITOR'S ACRONYM(S) ONR BD253		
				11. SPONSOR/MONITOR'S REPORT NUMBER(S)		
12. DISTRIBUTION/AVAILABILITY STATEMENT Distribution Statement A. Approved for public release; distribution is unlimited						
13. SUPPLEMENTARY NOTES						
14. ABSTRACT Reactive material composed of tungsten and aluminum are investigated computationally with respect to their suitability as warhead materials. The objective is to identify a material that has sufficient strength to survive the explosive launch from the warhead, has the capability of perforating a target, and fragments into fine particles upon target perforation, thereby enabling a combustion reaction. The considered materials are modelled on the mesoscale, i.e. by resolving the granular structure. Mesoscale simulations are carried out for a variety of different microstructures under explosive and impact loading. The simulation results are evaluated with respect to the fragment size distributions and relations between mesoscale parameters, launch and impact conditions and fragmentation characteristics are deduced. The simulations make use of a scaling on the macro-scale which is necessary to reduce the computational effort to a feasible amount. The validity of the scaling approach is analyzed. A suitable material is suggested.						
15. SUBJECT TERMS						
16. SECURITY CLASSIFICATION OF: a. REPORT b. ABSTRACT c. THIS PAGE			17. LIMITATION OF ABSTRACT		18. NUMBER OF PAGES 85	
					19a. NAME OF RESPONSIBLE PERSON Arno Klomfass	
					19b. TELEPHONE NUMBER (Include area code) ++49-761-2714-313	

Reset